Superhydrophobic Surfaces

A study of the superhydrophobicity of modified silicon dioxide surfaces

Authors

Anders Søbye
Jannick Kjær Jørgensen
Marie-Louise Knop Lund
Martin Okkerstrøm Mikkelsen

AALBORG UNIVERSITY
STUDENT REPORT

School of Engineering and Science
Aalborg University 2015
Group 4.205

AALBORG UNIVERSITY
STUDENT REPORT

Fifth Semester, School of Engineering and Science
Nanotechnology
Skjernvej 4A
9220 Aalborg Ø
http://www.nano.aau.dk

Title:

Superhydrophobic Surfaces

Project:

P5

Project Period:

September 2015 - January 2016

Projectgroup:

4.205

Participants:

Anders Søbye
Jannick K. Jørgensen
Marie-Louise K. Lund
Martin O. Mikkelsen

Supervisors:

Peter Fojan
Leonid Gurevich

Printed Copies: 7
Total Page Number: 59
Appendix: 0
Finished: January, 2016

Abstract:

The motivation of this project was to fabricate a superhydrophobic surface utilizing silicon dioxide as substrate. A double layer of silicon dioxide nanoparticles (SNPs) with mean diameters of 22 nm will be utilized to obtain sufficient roughness, and trichloro(1H,1H,2H,2H-perfluorooctyl)silane (PFOTS) will be utilized as a surface free energy lowering chemical. SNPs were characterized by atomic force microscopy (AFM), revealing the highest count of particle diameters at 15 - 30 nm, and wafers were prepared by ultrasonic and ozone cleaning. Three types of wafers were prepared. Wafers were coated with a monolayer of PFOTS deposited by chemical vapour deposition, double coating of SNPs, and a double coating of SNPs coated with a monolayer of PFOTS, respectively. Each deposition step was characterised by AFM and contact angle (CA) measurements. Furthermore, it was decided to expose the deposited SNPs to ozone in order to compensate for inconsistent CAs. Ultimately, deposition of SNPs increased hydrophilic characteristics of the silicon dioxide wafers, and deposition of PFOTS significantly increased hydrophobic characteristics of the wafers. The combination of SNPs and PFOTS resulted in highly hydrophobic properties of the wafers, but not superhydrophobic as intended. The resultant CAs were 130.10° - 139.29°, which was a significant increase compared to those with only PFOTS.

Preface

This project is written by group 4.205 consisting of fifth semester Nanotechnology students of Aalborg University from September 2nd to January 4th. Lector Peter Fojan and Lector Leonid Gurevich are the primary supervisors. The topic of this project is fabrication of nanostructures. This project will concern artificial superhydrophobic surfaces created through surface modifications.
This project will introduce the topic of superhydrophobicity. Furthermore, it includes a State of the Art chapter, which concerns the current production and application of superhydrophobic surfaces. The project includes theoretical chapters describing superhydrophobicity, introduction of PFOTS, and cleaning of wafers. A description of the experiments and results will follow, leading to a discussion and conclusion of the experiments according to relevant theory.
Throughout this project, each chapter and section will have numbered titles. Furthermore, all figures, significant equations, and tables will be numbered. The reference system applied is the numerical system and every reference is then represented by a [number], which refers directly to a specific source in the bibliography. Figures with no reference are composed by the group itself, and vectors will be denoted in bold.

Anders Søbye

Jannick Kjær Jørgensen

Marie-Louise Knop Lund

Martin Okkerstrøm Mikkelsen

List of Abbreviations

AFM:	Atomic Force Microscopy
CA:	Contact Angle
CAH:	Contact Angle Hysteresis
CVD:	Chemical Vapour Deposition
PFOTS:	Trichloro(1H,1H,2H,2H-perfluorooctyl)silane
UV:	Ultraviolet
SA:	Sliding Angle
SNP:	Silicon Dioxide Nanoparticle
RMS:	Root Mean Square

Table of Contents

1. Introduction

Hydrophobicity and superhydrophobicity with self-cleaning properties are well-known characteristics of some natural surfaces. The best known example is the leaves of the sacred lotus plant (*Nelumbo nucifera*) [1, 2], where electron microscopy of the leaf surface has revealed protruding 10 µm nubs covered with 0.2 - 2 µm wax crystalloids providing a two-scale roughness. [1, 3]
It is well accepted that with the combination of micro- and nanometer scale roughness, along with low surface energy materials, one can obtain surfaces with contact angles (CA) above 150° and sliding angles (SA) below 5° [4]. These surfaces have extraordinary self-cleaning and anti-adhesive properties, and are denoted superhydrophobic surfaces. [1]
However, multi-scale roughness may be a dominant factor, since the sacred lotus leaves utilize two-scale roughness, and have no extremely low surface energy interface. Nature does not rely on the low surface energy of $-CH_3$ groups or fluorocarbons, but can still achieve superhydrophobic effects on lotus leaves by wax crystalloids predominantly containing $-CH_2-$ groups. [1]
The ability to control the topography of surfaces has great potential in many fields of technology. For instance, controlling the wetting and self-cleaning of surfaces is of interest when fabricating satellite dishes, solar energy panels, green houses, etc. [1]. Furthermore, non-wettable surfaces may also prevent adhering of frost [1], which may have applications in most space-technologies and on glass surfaces in vehicles and flying machines.
In order to chemically modify the surfaces and achieve low energy properties, chemicals such as fluorinated polymers are of particular interest due to their extremely low surface energy. Studies even suggest that simply stretching such polymer films lead to superhydrophobicity [1]. Surface roughness can be achieved by techniques such as photolithography etching [5], growth of carbon nanotubes [5], etching of polymers [3], sol-gel processes [6], layer-by-layer self-assembly [7], etc..
This project will utilize silicon dioxide wafers as substrate for fabrication of superhydrophobic surfaces. Furthermore, a double layer of silicon dioxide nanoparticles (SNP) with mean diameters of 22 nm will be utilized to obtain sufficient roughness, and PFOTS will be utilized as the surface energy lowering chemical.

2. State of the Art

Hydrophobic and superhydrophobic surfaces have in later years received interest by the industry. Primarily considering self-cleaning and water repelling properties, but it may also prove useful considering different aspects, such anti-icing properties of surfaces.
Hydrophobic coatings have already found several applications in everyday life. The most commonly known application is probably the use of polytetrafluoroethylene (PTFE) for non-stick coatings in cookware by companies such as Tefal. The reason for its use in non-stick cookware is, however, most likely due to a friction coefficient, as low as 0.05, measured against polished steel [8].
It is already possible to buy hydrophobic coatings for industrial or consumer use from companies such as Aculon Inc., Ultratech International Inc., and P2i Ltd.. Aculon Inc. makes liquid repellant coatings by employing a monolayer of self-assembled phosphates to impart surface properties [9]. The phosphonate head groups form covalent bonds with the substrate while the tails can have different chemical groups in order to induce different surface properties to the substrate [9]. Aculon Inc. produces both hydrophobic, superhydrophobic, and oleophobic coatings, which can be applied to various products, such as optical components, smartphone displays, cutting razors, needles, and syringes.
Ultratech International Inc. has developed a superhydrophobic and oleophobic nanocoating that repels liquids because of a molecular structure that traps a layer of air on the surface, thus preventing the liquids from contacting the surface [9]. The product uses a two-layer coating, where both layers can be spray coated onto the surface, which increases the abrasion resistance of the coating [9]. The superhydrophobic coating by Ultratech International Inc., Ultra-Ever Dry®, can be applied to a wide range of substrates, such as metals, cinder, textile fabrics, and glass, although it gives a slight discoloration, and is only available for industrial use at the time.
P2i Ltd. has developed a process to apply an engineered nanoscale fluorocarbon-polymer coating by using pulsed-plasma vapor deposition. The coating forms a vertical structure with CF_3 groups pointing outwards, giving a surface free energy lower than that of PTFE, thus making the coating both hydrophobic and oleophobic. The coating is applied to finished products inside a vacuum chamber using a two-stage plasma polymerization process. First a radio-frequency plasma removes contaminants, that could disrupt bonding with the coating, from the surface of the products and creates free-radical sites for the coating to react with. Next a vapour of fluorocarbon monomers is introduced and a pulsed radio-frequency plasma is used to polymerize it and bond it to the free-radical sites on the surface. The low pressure in the chamber allows the monomer to permeate into all areas of the product, so that the polymer coats all surfaces, both externally and internally, resulting in a coating just a few nanometers thick. The technology is primarily used to protect electronics, such as mobile devices, as it makes them water-resistant and can even protect them when submerged. More than 100 million devices have already been produced with this coating. [9]

Although several uses of hydrophobic and even superhydrophobic surfaces have found its way into industry in order to induce self-cleaning or anti-wetting properties, research is still being conducted into creating superhydrophobic surfaces using different methods [10, 11, 12, 13].
In a study conducted by Yuan *et al.* superhydrophobic linear low-density polyethylene (LLDPE) was prepared and its self-cleaning properties and durability was tested [10]. LLDPE resin was dissolved in xylene and deposited on a cleaned glass substrate, where it was left to dry. When dried at 120 °C,

a smooth LLDPE surface was obtained with a water CA of 102 ± 1.8°. In order to increase the CA, the surface roughness was enhanced by drying at a temperature of 5 – 10 °C. The low temperature resulted in a slow evaporation of the solvent, which caused a phase separation, creating pores in the upper part of the LLDPE. The CA was then increased to 127 ± 2.1°. In efforts to make the surfaces superhydrophobic, the surface roughness was further enhanced by adding ethanol to the LLDPE solution. The ethanol acted as a precipitator, causing some LLPDE aggregates to appear, which again acted as nuclei for further LLPDE aggregation. This resulted in further phase separation and thus further enhanced surface roughness. The CA was now 153 ± 2°,the SA was 10°, the surface was 99 % efficiently self-cleaning, and it was stable after one month in storage and under large variations in pH values and temperatures. [10]
In view of the self-cleaning properties of superhydrophobic surfaces, Su *et al.* prepared an optically transparent superhydrophobic film that could be deposited on glass, such as windows and car windshields, thus making them self-cleaning. The superhydrophobic surface was prepared by spincoating a solution of epoxy onto the glass after which a suspension of SNP was spincoated onto the surface. The surface was now dried for 8 hours at 100 °C, followed by soaking in a 0.5 wt. % perflouroalkyltriethoxysilane (PFO) suspended in a ethanol solution followed by a second drying at 100 °C for 12 hours. [11]
For a 1.0 wt. % SNP suspension, the CA and SA were 168° and 11.8° respectively, whereas for a 0 wt. % SNP suspension, the CA and SA were 105° and >30° respectively, indicating that although the PFO coating resulted in a hydrophobic surface, it was necessary to embed SNPs in the coating, thereby enhancing surface roughness to achieve a superhydrophobic surface. Furthermore, the superhydrophobic surface was shown to have a transmittance of more than 99 % for light with a wavelength of 500 nm, making it ideal for transparent surfaces such as windows or car windshields. [11]
For large-scale production of superhydrophobic surfaces, one-step methods are very promising, because of the simplicity in both process and equipment. Wang *et al.* used a one-step method to create superhydrophobic surfaces on various substrates including textile fabrics, electrospun nanofibre mats, filter paper, glass slides, and silicon wafers. A sol solution containing SNPs was prepared by co-hydrolysis and condensation of two silane precursors, tetraethylorthosilicate and tridecafluorooctyl triethoxysilane, in a hydrous ammonia ethanol solution. The sol solution can easily be coated onto different substrates forming a transparent film simply by dipping, spraying, or spin coating. SNPs ranging from 50 – 150 nm in diameter, covered in fluorinated carbon species, will randomly form aggregates on the surface, thus both decreasing surface free energy and increasing roughness. When coated onto a polyester surface a CA and SA of 174 ± 2.7° and 2.2 ± 0.1°respectively was obtained. [12]
Another one-step method was developed by Onda *et al.* who created a fractal surface. Alkylketene dimer (AKD) solid films were grown with a thickness of 100 µm on glass substrates. A glass substrate was dipped into melted AKD at 90 °C, then cooled to room temperature in the ambience of dry nitrogen gas. When AKD solidifies it undergoes a fractal growth thus resulting in a fractal surface. For this surface a CA as large as 174° was achieved, whereas for a flat AKD surface a CA of only 109° was achieved. [13]

Creating anti-icing or icephobic surfaces is also of great interest, as it could prevent icing on planes or prevent glaze from forming under freezing rain. If spread over a surface, even a thin layer of ice, can bring down power lines, burst pipes, make roads impassable, and cause loss of lift on aircraft wings [14]. Superhydrophobic surfaces are, however, not necessarily icephobic, because the mechanisms of water and ice adhesion are different [15].
Accumulated ice is so sturdy, that large-scale breaking is very difficult. For severe ice accumulation,

even the pneumatic boot, designed to break ice of aircraft wings and stabilizers, struggles. Common to all methods for dealing with ice, is that they are either resource intensive, damaging to the environment, or not reliably up to the task. [14]
Although superhydrophobic surfaces does not necessarily have the ability to shed ice after formation or prevent ice formation from static water droplets [15], it can prevent ice formation if dynamic water droplets bounce off at impact before ice nucleation can occur [14].
Mishchenko *et al.* have investigated the movement and freezing of dynamic droplets impacting a superhydrophobic surface of temperatures below freezing. The superhydrophobic surface was produced by creating ordered surface structures on micrometer scale, in order to create surface roughness, followed by a coating with a hydrophobic silane species. For comparison, a substrate without the surface structure, but with the silane coating was used as a hydrophobic surface and a flat aluminium substrate was used as a hydrophilic surface. The substrates were cooled to -10 °C and tilted to an angle of 30°. Water at 0 °C was poured on the substrates at a rate of 0.06 mL/sec from a height of 10 cm above the substrate. After 10 minutes, ice had accumulated on both the hydrophilic and hydrophobic surface, whereas no ice had accumulated on the superhydrophobic surface. When only a single droplet was dropped on the tilted substrates, the droplet would freeze when the substrate temperature was below 0 °C for the hydrophilic and hydrophobic surfaces, whereas for the superhydrophobic surface, the droplet would bounce off at substrate temperatures as low as -25 °C, even at 0° tilt. The droplet would, however, freeze immediately upon impact at substrate temperatures at -30 °C, even with a tilt angle of 15° and a droplet temperature of 20 °C. This droplet would, however, freeze in a Cassie-Baxter state, making removal of the ice easier. When the droplet was supercooled to -5 °C before impact, the superhydrophobic substrate needed a temperature as high as -15 °C in order to prevent the droplet from freezing. [14]
In contrast to typical disordered superhydrophobic surfaces, the ordered and uniform surface structure prevented pinning and freezing of impacting droplets. Furthermore, experiments carried out in 40 – 60 atm, showed that the CA of a water droplet did not change on superhydrophobic substrates with closed-cell surface structure, in contrast to experiments done at 1 atm. This implies that such a surface should be able to retain superhydrophobicity upon impact with droplets traveling at 90 – 135 m/s, as the air becomes trapped, upon impact, in the closed cell structure. Furthermore, the continuity and structure of a closed-cell pattern will render it mechanically robust. This technology shows great promise in giving substrates anti-icing properties regarding impacting dynamic water droplets as experienced by freezing rain or water droplets impacting on aircrafts. [14]

As is evident from this chapter, superhydrophobicity is a widely used technology, that has the potential to solve a large variety of problems that arises from the adhesion of water to surfaces.

3. Hydrophobicity

At its core, hydrophobicity arises when a molecule does not partake in the hydrogen bonding of water [16]. When a hydrophobic particle is submerged in water, it will create a volume where the density of water vanishes [16]. This chapter will focus on hydrophobic and superhydrophobic surface in the context of both surface free energy and surface roughness.

3.1 Surface Free Energy

Surface free energy has multiple definitions in literature, which differs between liquids and solids [17, 18]. Surface free energy can be seen as work resulting from adhesive forces at the surface including van der Waals forces, and hydrogen interactions [17]. Surface free energy can be defined using the example of two separate materials in contact with each other. Between the surfaces, adhesive forces are present and work is needed to overcome these forces in order to separate the two materials. When the two materials are separated, two new surfaces are essentially created, thus the work needed to overcome the interfacial adhesive forces has effectively created new surface areas. Surface free energy is then the energy required per unit area to create a surface. [18]
Surface free energy can also be explained by a droplet of water surrounded by vapour, not experiencing gravity, see Figure 3.1.

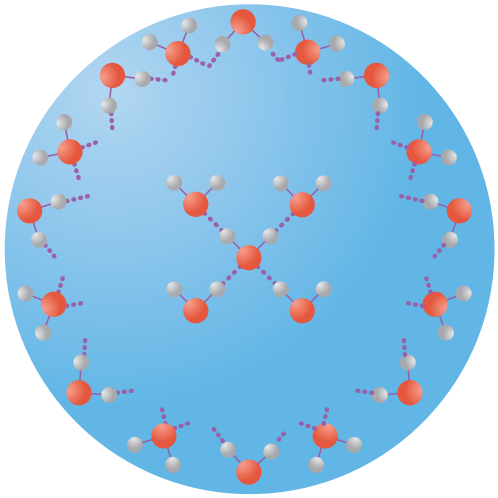

Figure 3.1: Illustration of surface free energy in a water droplet. The free energy is minimized when water molecules are hydrogen bonded (dotted lines) to four other water molecules as is the case with the center water molecule [19] in the illustration. However, the molecules at the surface can not achieve four hydrogen bonds. This drives the water molecules to minimize surface area, thus minimizing the total free energy of the droplet. As the sphere is the geometric shape with the smallest surface-to-volume ratio, it becomes the natural shape of water droplets, when no external forces are present.

Liquid water is highly ordered compared to other liquids due to short-range hydrogen bonding networks. Ideally a water molecule in the center of the droplet has four closest neighbours, which are connected tetrahedrally by hydrogen bonds, see Figure 3.1 [19, 20]. The center water molecule is being pulled equally by the hydrogen interactions on both sides of the molecule, thus the net force is zero. The same effect is occurring on the surface of the water droplet, but the surface water molecules lack some of their neighbours, giving a net force pulling the molecules towards the center of the water droplet. This

drives the droplet to minimize its surface area resulting in the spherical shape of the droplet, which is the most thermodynamically favourable shape due to it having the smallest surface-to-volume ratio. [21]
When dealing with liquids another definition of surface free energy becomes useful, namely the surface tension which can be defined using Figure 3.2.

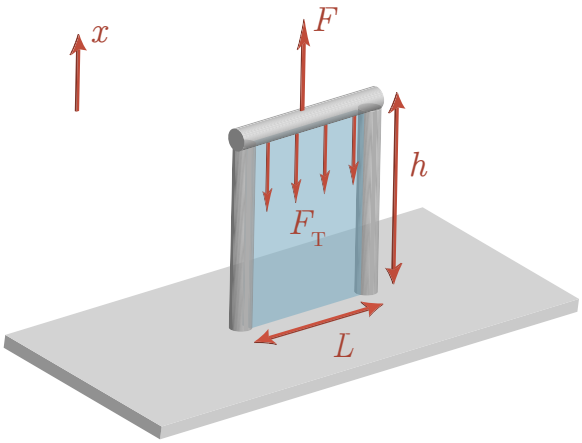

Figure 3.2: A liquid film is drawn on a frame of height h with a bar of sidelength L being dragged with a force F, creating new surface areas. The liquid creates the new surfaces by moving molecules from the inside of the film and out to the edges instead of increasing the intermolecular distances. The liquid back and front surfaces are resisting to an increase of surface area described by the surface tension resulting in a reactionary force F_{T}.

In Figure 3.2, a liquid film is drawn out of a frame, where one side with length L can be pulled in the x-direction with force F. The liquid film has a back and front surface and the film itself is rather thick in molecular terms, meaning it has an inside consisting of molecules not residing on either surface of the film. The water film would thus have molecules on the inside with 4 hydrogen bonds each and molecules on the surface lacking some of these bonds. As the frame area is increased by

$$\Delta A = \Delta x \cdot L,$$

the liquid film must follow. But rather than increasing the intermolecular distance as an elastic spring, the film begins to shrink in thickness as the inner molecules begin to become part of the new surface areas. As explained earlier about the water droplet, the molecules on the surface lack the desired number of hydrogen bonds, thus increasing the surface free energy. This energy originates from the work W used to lift the side given by

$$W = \Delta x \cdot L \cdot \gamma, \tag{3.1}$$

where γ is the surface tension [22]. Since $W = F \cdot \Delta x$, Equation (3.1) becomes:

$$F_{\mathrm{T}} = L \cdot \gamma. \tag{3.2}$$

Isolating the surface tension in Equation (3.2) makes it clear that the unit of surface tension is force per unit length. Following Equation (3.3),

$$\text{Surface Free Energy} = \frac{[\mathrm{J}]}{[\mathrm{m}^2]} = \frac{[\mathrm{N} \cdot \mathrm{m}]}{[\mathrm{m}^2]} = \frac{[\mathrm{N}]}{[\mathrm{m}]} = \text{Surface Tension}, \tag{3.3}$$

surface tension is the surface free energy of the liquid, as they share dimensions.

When a water droplet is placed on a surface, several interfacial surface tensions are now in effect as shown in Figure 3.3.

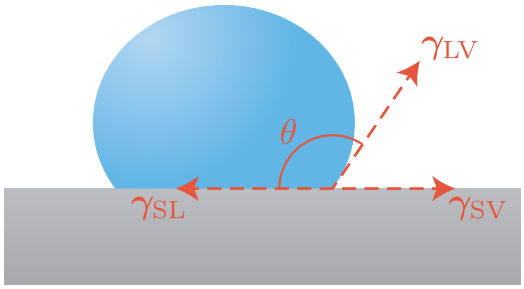

Figure 3.3: Illustration of the three interfacial surface tensions that are in effect at the triple contact line, when a droplet rests on a surface, namely γ_{LV} (liquid-vapour), γ_{SL} (solid-liquid), and γ_{SV} (solid-vapour). θ is the CA.

The point of interest is the triple contact line where the three phases interact [23, 24, 25]. At the triple contact line there is interfacial tension between liquid and vapour (γ_{LV}), liquid and solid (γ_{SL}), and solid and vapour (γ_{SV}). From Figure 3.3 it is evident that the free energy of the system is minimized when the surface tension components in the surface plane cancel each other out, meaning the total surface tension is zero in mechanical equilibrium [23]. Thus

$$\gamma_{SV} - \gamma_{SL} - \gamma_{LV} \cdot \cos(\theta) = 0, \tag{3.4}$$

with θ being the CA. Rearranging Equation (3.4) gives the common form of Youngs equation [26, 27],

$$\cos(\theta) = \frac{\gamma_{SV} - \gamma_{SL}}{\gamma_{LV}}. \tag{3.5}$$

The validity of Equation (3.5) has been questioned due to, in part, the various effects of gravity by Liu *et al.* [23, 28, 29]. Another point of criticism has been, that forces acting in the plane perpendicular to the surface, see Figure 3.3, must be balanced by stress in the surface. This is supported by the fact, that water droplets can cause curling of mica sheets [28, 30], which conforms with the theories postulated by Bikerman *et al.* [31]. This has lead Eustathopoulos *et al.* [30] to conclude that the once thought equilibrium, proposed by Young, is only a metastable state. Furthermore, Liu *et al.* state that experiments on a space shuttle has disproven Youngs equation [28], but Garandet *et al.* has studied a droplet in a system with minimzed free energy, and they found that the CA is still determined by Youngs equation [32]. Regardless of the aforementioned criticism of Youngs equation, it will be utilized as a theoretical basis in this project.
Youngs equation is an equilibrium condition of the system which gives a measurable parameter, the CA. This has made it a tool for measuring the surface free energy of solids in the literature [17]. It is clear, that for the greatest CA, 180°, the fraction on the right-hand side in Equation 3.5 must become negative one. It can be predicted what conditions would increase the CA. If the droplet extends the triple contact line, more atoms of the surface will be covered by the water droplet. If the surface free energy of the solid is higher than the surface free energy of the liquid, the total energy of the system decreases. If, on the other hand, the surface free energy of the solid is lower than that of water, it is unfavourable for the droplet to make contact with the solid and the CA increases. [23]

3.2 Wetting States

Youngs equation assumes a completely flat surface, but roughness also plays a role in hydrophobic surfaces. A definition of hydrophobicity is a CA above 90°, while a CA above 150° can define a

superhydrophobic one [26, 33]. Wenzel [34] proposed a modification to Youngs equation based on the Wenzel state. The Wenzel state assumes that when a droplet is placed on a rough surface, the water droplet fills the asperities of the surface, see Figure 3.4. The roughness parameter r of the surface can be seen as the factor with which the actual surface area increases compared to the projected area of the surface. The roughness is thus

$$\frac{A_\mathrm{r}}{A_0} = r, \text{ where } r > 1, \tag{3.6}$$

A_r is the actual surface area, and A_0 is the projected surface area. r is proportional to the root-mean-square (RMS) roughness, of the surface [34, 35, 36]. RMS is found using Equation (3.7)

$$\mathrm{RMS} = \sqrt{\frac{1}{N}\sum_{j=1}^{N} r_j^2}. \tag{3.7}$$

In Equation (3.7), N describes the number of deviations from the projected surface area, and $r_j = z_j - \bar{z}$, where z_j is the height of the deviation, and $\bar{z}$ is the mean value of the surface. Equation (3.7) describes the RMS value of the measured height deviations from the mean value. [3]
Due to the increase of the actual surface area, the original surface tensions, which are dependent on the surface area, must be multiplied by r in Equation (3.5), giving rise to a new angle,

$$r \cdot \cos(\theta) = r \cdot \frac{(\gamma_\mathrm{SV} - \gamma_\mathrm{SL})}{\gamma_\mathrm{LV}} = \cos(\theta^*). \tag{3.8}$$

The angle θ^* is the apparent CA. An interesting point, in relation to the Wenzel state, is that the roughness enhances whichever state the flat surface is in. If the original surface was hydrophilic, meaning $\cos(\theta)$ is positive, r would give an increase in hydrophilicity. If the original surface was hydrophobic, meaning $\cos(\theta)$ is negative, r would give an increase in hydrophobicity. [37]
However, it is worth noting that Equation (3.8) is only valid as long as $-1 \leq r \cdot \cos(\theta) \leq 1$.
The Wenzel model assumes a complete surface connection between droplet and surface, yet another state is possible [26]. In the Cassie-Baxter model the surface has a particular roughness, which allows vapour to be trapped beneath the water droplet as seen in Figure 3.4.

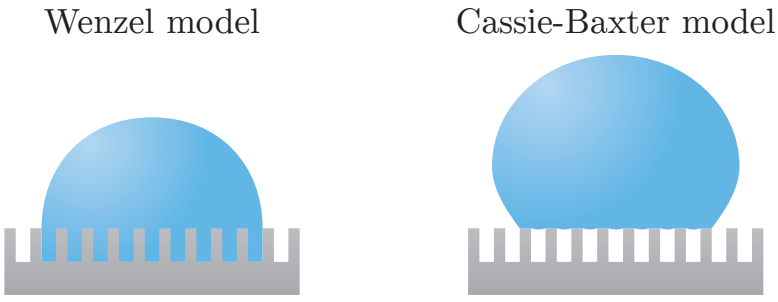

Figure 3.4: Illustration of the Wenzel and Cassie-Baxter models. The Wenzel model assumes the water droplet fills the asperities of the surface, while the Cassie-Baxter model assumes the droplet is in contact with some fraction of solid and some fraction of vapour trapped beneath the droplet. Inspired by Martines *et al.* and Li *et al.* [26, 38].

The Cassie-Baxter model, as shown in Figure 3.4, concerns the situation where the droplet rests on top of a combination of vapour and the original surface. The vapour fraction f_v and original surface fraction f_s of the total surface area is multiplied by the cosine of the CA of the solid and the cosine of the CA of vapour θ_v, respectively, see Equation 3.9

$$f_\mathrm{s} \cdot \cos(\theta) + f_\mathrm{v} \cdot \cos(\theta_\mathrm{v}) = \cos(\theta^*). \tag{3.9}$$

The CA contribution from the solid is just the CA of the original surface, multiplied by f_s and r. As a water droplet in vapour is completely spherical, the CA of vapour is 180° giving a CA contribution of negative one. This gives the cosine of an apparent CA of

$$r \cdot f_s \cdot \cos(\theta) - f_v = \cos(\theta^*). \tag{3.10}$$

Increasing f_v gives a more hydrophobic surface thus increasing the apparent CA.

According to Berthier *et al.*, it can be derived, that there exists a CA, such that the droplet goes from a Wenzel to a Cassie-Baxter state [39, 40].
The case can also be, that the droplet exists in a meta-stable Cassie-Baxter state, as shown by Bico *et al.*, where the droplet needs additional energy in order to enter the Wenzel regime [41]. Murakami *et al.* states that under certain conditions the Cassie-Baxter state is a meta-stable state, which, if provided energy equal to the energy barrier, can transform into a Wenzel state. The energy can be provided by several external factors, such as thermal or mechanical factors. The transition is reported to be a reversible one, if thermodynamic factors are changed such that both states are stabile. [42, 43]
Reality does not, however, correspond to a two-state system entirely. As Giacomello *et al.* have shown, there is actually a second Cassie-Baxter state that differs slightly from the traditional Cassie-Baxter state [44].

3.3 Sliding Angle and Contact Angle Hysteresis

When investigating whether a superhydrophobic surface is in the Wenzel state or the Cassie-Baxter state it can become quite difficult to determine based on CA alone. Both states enhance the hydrophobic effect of hydrophobic surfaces, while the Wenzel state enhances hydrophilicity of hydrophilic surfaces as mentioned in Section 3.2. However, it can be quite difficult to see the lowered CA of a hydrophilic surface, if it was enhanced by a Wenzel state, as CAs below 10° are quite difficult to measure. Furthermore, some properties of superhydrophobic surfaces, such as self-cleaning, are difficult to determine by CA measurements alone [5, 26]. Consequently, another method to differentiate between the two states could be of use. One such method could be the measurement of contact angle hysteresis (CAH) as shown in Figure 3.5.

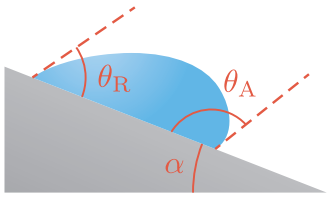

Figure 3.5: CAH is the difference between the advancing angle θ_A and the receding angle θ_R when a droplet is placed on a surface tilted with an angle α.

A water droplet is placed on a surface and the surface is tilted until the droplet starts moving at the SA α, at which point the advancing angle θ_A and receding angle θ_R is measured [5]. The difference between these angles is termed the CAH ΔH, see Equation (3.11) [45]

$$\Delta H = \theta_A - \theta_R. \tag{3.11}$$

CAH is useful for differentiating between the surface states, as a high CAH indicates a Wenzel state, and a low CAH indicates a Cassie-Baxter state [36, 44, 45, 46, 47, 48, 49]. Bravo *et al.* even argues that it is impossible to achieve ideal superhydrophobic characteristics of a surface, with CA above 150°

and CAH below 10°, in a Wenzel state, since droplets are easily pinned to the surface and unwilling to roll off [7].
CAH also becomes an important tool in determining the self-cleaning properties of a surface. The CAH essentially goes to zero at high RMS values for ideal self-cleaning surfaces. Furthermore, a self-cleaning surface utilizes water droplets sliding over it, absorbing contaminants, however the droplet is required to act as an elastic ball rather than a fluid [26], see Figure 3.6. For this effect to occur, a small CAH is required according to Xiu [5]. On a non self-cleaning surface the droplets merely pushes the contaminants aside, as shown in Figure 3.6. [26]

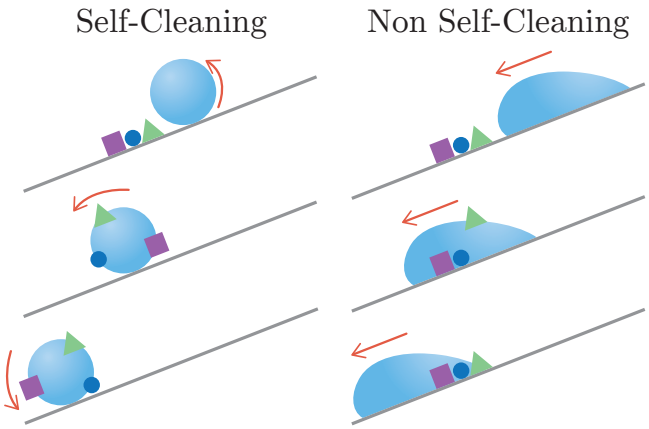

Figure 3.6: Self-cleaning surfaces are characterized by small CAH as droplets on these surfaces tend to act as elastic balls, rather than fluids as is the case of non self-cleaning surfaces. On self-cleaning surfaces the contaminants represented by the small square, circle, and triangle are absorbed by the ball-like water droplet, while the liquid water droplets on non self-cleaning surfaces are unable to absorb the contaminants. Inspired by Li *et al.* [26].

4. Trichloro(1H,1H,2H,2H-perfluorooctyl)silane

In order to fabricate superhydrophobic surfaces that are anti-adhesive, coating by materials that posses low surface free energy are of interest. Those materials include fluorocarbons, different organic polymers, and inorganic oxides such as ZnO and TiO_2 [50]. Fluorocarbons, such as organic silanes, are widely applied in the fabrication of hydrophobic and superhydrophobic surfaces as they provide the necessary low surface free energy, surface coverage, and surface distribution. A successful hydrophobic coating eliminates hydrogen bonding by shielding polar sites from interactions with surrounding water, thus creating an apolar interface. Silanol groups are a common site for hydrogen bonding, and reside on the surface of oxidized silicon wafers. However, the hydrogens of the hydroxyl groups can be eliminated by oxane bond formation with organic silanes, inducing hydrophobicity by eliminating hydrogen bonding sites and providing an apolar interface consisting of the apolar fluorinated hydrocarbon substituents of the organic silanes. [50]
PFOTS, see Figure 4.1, is an organic silane that forms self-assembled monolayers. As other silanes, PFOTS can modify surfaces by forming the monolayers under anhydrous conditions, which is consistent with CVD requirements, thus it is easy to apply organic silanes during fabrication of hydrophobic surfaces. Although a monolayer is desired, multilayer adsorption occurs to some extent by most deposition techniques. [50]
During vapour deposition, 5 % PFOTS will normally be suspended in solvents as toluene or tetrahydrofuran [51]. When performing CVD, non-hydroscopic solvents are of interest as polymerization of PFOTS is unfavorable during the process [51]. Hydroscopic solvents often include solvents containing hydroxyl groups [52] and solvents in which water has a high solubility. This makes alcoholic solvents a poor choice for CVD [53]. Furthermore, solvents must display volatility in order to enable fast and effective vaporization of PFOTS.

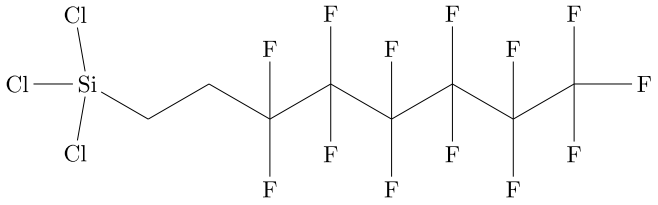

Figure 4.1: Schematic representation of PFOTS ($CF_3(CF_2)CF_2CF_2{-}SiCl_3$).

During CVD, the amount of atmospheric air in the chamber is minimized in order to hinder undesirable side reactions, and a noble gas is infused as they are inert and often heavier than atmospheric air. This creates an inert environment around the substrates, which induces reactions between PFOTS and the substrate. During the drying process of CVD, PFOTS is vaporized in the chamber along with the solvent. One or multiple highly electronegative chloride atoms, of the vaporized PFOTS, form hydrogen bonds with the hydrogen atom of the silanol groups of the substrate, and the nucleophilic substitution continues. Chloride is an excellent leaving group [54] due to its stable ionic form, thus gaseous hydrogen chloride is released and a strong covalent bond will form between silicon of PFOTS and the oxygen of the silicon dioxide, see Figure 4.2 [50, 51]. Either of the three chlorides of PFOTS can participate in the reaction, however, the distribution may become random, and unreleased chloride atoms

may act as leaving groups during temperature elevation or reaction with vaporized water [51] forming inter-covalent bonds between PFOTS molecules, polymerizing PFOTS, see Figure 4.2. However, the reaction is still under debate, and covalent bonding is only one of the possible processes, where lateral polymerization of absorbed silanes or three-dimensional polymerization are also proposed processes [50].

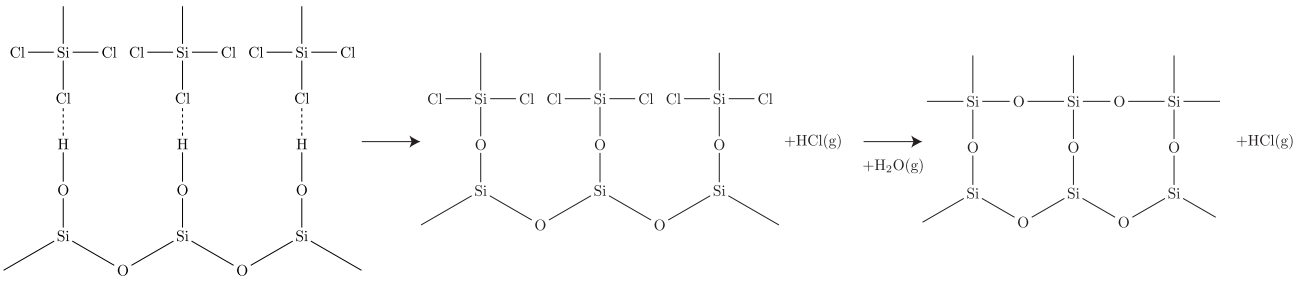

Figure 4.2: Schematic representation of PFOTS covalently bonding to silanol groups of the substrate during CVD. Highly electronegative chloride ions of PFOTS form hydrogen bonds with the silanol groups of the silicon dioxide surface, releasing hydrogen chloride as an oxane bond is formed. After CVD a reaction with water vapour induces polymerization of PFOTS. Inspired from W. R. Grace & Co.-Conn. [55, 56] and Gelest, Inc. [51].

The hydrophobic effect of PFOTS is attributed to the fluorine atoms of the molecule. Although fluorine has the highest electronegativity of all the elements, and its bonds tend to be very polar, it has a very low polarizability [19]. Furthermore, the three lone pairs of fluorine in the carbon-fluorine bond are highly reluctant in getting involved in resonance structures or interactions like hydrogen bonding [57]. Thus, fluorine is a very poor leaving group, especially in S_N2 reactions, and it is difficult to ionize. Furthermore, CF_3 groups are generally less attacked by electrophilic reagents [19], and due to the small size of fluorine, it easily replaces hydrogen in molecules. The carbon atom is thereby effectively shielded from reagents [19], which, along with the extreme electronegativity of fluorine, maximizes the electrostatic stabilization of heavy fluorine-containing molecules like PFOTS. Furthermore, the carbon-fluorine bond can be considered effectively oxidized, and has, as a result, no tendency for oxidization reactions [19].

5. Cleaning of Silicon Dioxide Wafers

When fabricating on the micro and nano scale, a substrate free of or with limited contamination is of great importance. Contamination of the substrate can originate from typical sources like production processes of the substrate, preparation processes, mechanical laboratory equipment, applied chemicals, or even the air. Types of contamination often include ionic materials typically from inorganic compounds that is adsorbed to the surface, silicon particles or metal debris from laboratory processes like dicing, or organic contaminant films and discrete particles from photoresist, solvent residues, or components from plastic storage containers [58]. Detached particles from dicing processes may be minimized by coating with photoresist. By principle, the photoresist polymer layer will be thick enough to cover all impurity cavities and microstructures of the wafer, thus protecting the underlaying substrate structure from vibrations and damage during the dicing process. [59]
In order to remove contamination species, different cleaning techniques have been applied, and most involve wet-cleaning processes, and preferably will not introduce re-contamination or new contaminants. Thus, selection of appropriate cleaning processes and chemicals are essential to meet quality demands [60].
Original cleaning processes include two-step chemical etching by extremely alkaline and acidic solutions, and megasonic systems utilizing sonic waves of 850 - 900 kHz; often relying on hydrogen peroxide solutions. However, many of the original techniques are only useful for specific applications, and often introduce undesirable side effects including deposition of inorganic contamination particles or metals, and many of the techniques even cause damage to the surface of the substrate. Alternatively to these cleaning techniques, the wet-cleaning ultrasonic technique and dry-cleaning by ultraviolet (UV) radiation and ozone is of interest. [58]

The ultrasonic techniques primarily rely on high intensity sound waves with frequencies ranging from 20 - 80 kHz, that generate pressure fluctuations, which result in cavitation bubble production. The bubbles grow to a maximum size inversely proportional to the frequency of the ultrasonic waves. At 20 kHz, the size of the bubbles maximize around 170 µm in diameter, and decreases with increasing frequency [60]. As the bubbles violently collapse, they release enough energy to dislodge and disperse inorganic contamination particles. As a result, solvent molecules can encapsulate the particles, minimizing van der Waals attraction forces between the particles and the surface of the substrate. However, compared to megasonic techniques, ultrasonic techniques are much less effective for removing smaller particles, and cleaning efficacy decreases with decreasing particle size. Generally, ultrasonic techniques are great at removing particles with diameters larger than 300 nm [58], whereas particles with diameters smaller than 100 nm typically require a focused ultrasonic beam of high local intensity, especially if they are irregular in shape. Using this method, however, does not necessarily provide the sufficient energy and force for removal of the small particles [61]. Furthermore, ultrasonic techniques primarily rely on cavitation formation, where megasonic techniques primarily relies on micro-steaming flows. However, both effects are present at every frequency. [58, 61]
Attractive forces between solids predominantly cause adhesion of particles toward the substrate surface [62], and these forces become increasingly significant for small particles since the van der Waal attraction forces depends on the first power of the particle diameter while mechanical removal forces

vary with the third power of the particle diameter [62]. The forces of adhesion between particles and the substrate surface are typically 2 - 3 times lower in liquids than air, thus wet-cleaning techniques are particularly effective for particle removal. Furthermore, the adhesion forces are specific for the type of substrate, type and size of particles, and solvent conditions during wet-cleaning processes [62]. However, lodging effects can cause smaller particles to be more difficult to remove as they tend to be trapped in microstructures on the surface of the substrate [60].
Although ultrasonic waves result in mechanical removal of contaminant particles, it is important to apply a proper cleaning solvent in the process in order to obtain a successful cleaning without inflicting any damage to the substrate or equipment [60]. Effective and successful cleaning solvents are chosen based on properties like stability, solubility, reactivity, dispersion or encapsulation of solid residues etc., and the solvent must cavitate well with ultrasonic waves and be compatible with the substrate [60]. Furthermore, the cleaning solvent must prevent redeposition of the contamination particles. Aqueous solvents are universal and obtain great cleaning results, however, they must often be accompanied by additives like surfactants, which can encapsulate dislodged contaminant particles, preventing redeposition. Redeposition can also be prevented by applying apolar solvents in order to minimize van der Waals attraction forces between substrate and contamination particles. The cleaning chemical may also initiate dissolving of contamination species. [60]
Following wet-cleaning processes is immediate spray-rinsing, typically in propan-2-ol, where the remaining cleaning solvent containing contamination species is removed, and subsequent drying processes may preferably be mechanical rather than evaporation, as evaporation induces a risk of redeposition. [58, 60]

Dry-cleaning processes include ozone cleaning. The ozone cleaner is designed to eliminate organic surface contamination by employing the combination of gaseous ozone and UV radiation. Most often, a low pressure mercury arc lamp emits 90 % radiation at 253.7 nm and 5 % radiation at 184.9 nm at room temperature [63]. 184.9 nm radiation is absorbed by gaseous dioxygen, which generates ozone with atomic oxygen as intermediate, and 253.7 nm radiation is absorbed by ozone resulting in decomposition of the molecule into dioxygen with atomic oxygen as an intermediate. It is the constant formation and destruction of ozone that enables an effective cleaning process, since atomic oxygen is a very powerful oxidizing agent. In order to decompose a covalent bond by radiation, the energy of the radiation must exceed the bonding energy of the specific bond. The energy of 184.9 nm radiation exceeds the energy of most organic single and double bonds, and are absorbed by many organic compounds along with 253.7 nm radiation. The absorption of the radiation by organic molecules cause photochemical changes, generating excited molecules, free radicals, and dissociated molecules. It is suggested that atomic oxygen oxidizes the photolysed molecules, and the products of the reaction is most often water, carbon dioxide, or nitrogen gas, depending on the composition of the organic molecule. Every product of the oxidation process evaporates, leaving the surface free of organic contamination, where only traces have been identified. [63, 64, 65, 66]
It is especially the combination of UV radiation and ozone that is powerful. One study examined the decomposition of human oil on silicon dioxide wafers, and found that the combination of 253.7 and 184.9 nm radiation along with ozone resulted in total decomposition after 20 seconds. If only 253.7 nm radiation and ozone was used, the decomposition process was prolonged to 90 seconds. When only 253.7 nm radiation was used the decomposition process was prolonged to 1 hour, and if only ozone was present, the decomposition process was prolonged to 10 hours. [63]
The ozone cleaner can clean both mica, glass, silicon dioxide, and metal surfaces, and successfully oxidize and decompose most organic compounds including photoresist polymers, and destroy several bacteria and vira within minutes [67]. However, inorganic particles, dust, metals atoms, and salts are

expected to remain unharmed by the UV radiation and ozone [63], or oxidize more slowly [66]. However, such contamination species can be effectively removed by pre-cleaning of the wafers, including wiping in acetone [64]. Contamination originated from pre-cleaning including acetone, ethanol, propan-2-ol, methanol, and toluene are effectively oxidized and decomposed within 8 minutes of ozone cleaning [66]. Moreover, the substrate must have been successfully pre-cleaned in order to remove thick gross contamination, and the ozone cleaning process is capable of oxidizing inorganic compounds like metals to their final oxidation state, resulting in an oxidized layer of a few nanometers. Thus metal substrates, which should not be oxidized, should only be placed in the ozone cleaner for no longer than one minute. [63]
Furthermore, an ozone cleaned silicon dioxide wafer will have an contact angle around 4° [66].

6. Materials and Methods

Materials

- 10 mL Greiner tubes
- Petri dishes
- 1.6 mL semi-micro cuvettes (polystyrene) from Greiner Bio-one
- IMTEX Cellulose Polyester tissues
- 100 mm p-doped (100) Silicon wafer with 300 nm dry thermally oxidized silicon dioxide (University Wafers)
- Laurell spin coater WS-650S-23NPP/C2/IND
- Disco Automatic Dicing Saw DAD321
- Powersonic cleaning bath from Martin Walter Ultraschalltechnik AG
- Ultra violet ozone cleaner INC UV.TC.EU.003 from Bioforce Nanosciences
- Vacuum chamber and KNF Laboport vacuum pump for chemical vapour deposition
- Eppendorf Centrifuge 5804R
- NT-MDT Solver PRO scanning Probe Microscope including Nova 1.1.1 Revision and Gwyddion 2.41 software
- UV1 UV/Visible spectrophotometer from VWR International including Visionlite Fixed software
- Contact angle setup including IC Capture 2.1 and ImageJ software

Chemicals

- MICROPOSIT™ S1813™ G2 positive photoresist, multipurpose (DOW® Electronic Materials)
- Pure Acetone, 99,5% (Sigma Aldrich)
- Propan-2-ol, 99,9% (Sigma Aldrich)
- Trichloro(1H,1H,2H,2H-perfluorooctyl)silane, 97%, (Sigma Aldrich)
- Toluene, 99.9 %, (Sigma Aldrich)
- LUDOX® TM-40 colloidal silica, 40 wt. %, supension in water (Sigma Aldrich)
- Milli-Q water

6.1 Atomic Force Microscopy Measurements

Every AFM measurement in this project was performed in semi-contact mode using SCAN SENS HA-HR double rectangular silicon cantilevers with gold reflective coating. Side A of the cantilever had a resonance frequency of 380 kHz, a force constant of 34 N/m, and measured 3 µm in thickness, 34 µm in width, and 93 µm in length. Side B of the cantilever had a resonance frequency of 230 kHz, a force constant of 17 N/m, and measured 3 µm in thickness, 34 µm in width, and 123 µm in length. Side A of the cantilever was most frequently applied during AFM measurements. An octahedral monocrystalline silicon tip was applied. The last 200 nm of the tip was conic in shape with a cone angle of 30°. The curvature radius of the end of the tip was less than 10 nm.
Furthermore, the scan size was 5 x 5 µm and the scan rate was 0.3 Hz, scanning 512 x 512 points.

6.2 Chemical Vapour Deposition

CVD was performed in order to covalently link vapourized PFOTS to silicon dioxide forming a hydrophobic self-assembled monolayer, as described in Chapter 4. A solution of 10 % PFOTS suspended in toluene was prepared, and placed in the vacuum chamber along with the appropriate wafers. Afterwards, vacuum was obtained in the vacuum chamber by the connected vacuum pump, followed by the introduction of argon into the chamber until full. This step was done thrice. Vacuum was obtained once more in the chamber, followed by the introduction of a small amount of argon. Lastly, an incubation time of 45 minutes followed, initiating a chemical reaction between silicon dioxide and PFOTS. This procedure was applied during every CVD process in this project.

6.3 Preparation of Silicon Dioxide Wafers

The following preparation of wafers was performed in a clean room, designed for ISO class 5. Firstly, a 100 mm silicon dioxide wafer, supplied by University Wafers US, was spin coated with positive photoresist at 3000 RPM for 60 seconds, followed by heating at 110 °C for 60 seconds, in order to prepare the wafer for dicing. Afterwards, the wafer was diced in the (110) direction of the silicon dioxide into 1 x 1 cm wafers by the dicing saw. According to the supplier, the photoresist applied in this project results in a coating of approximately 1.20 µm in thickness, and are used for silicon and silicon dioxide substrates [68].
In order to strip the diced wafers of photoresist, and to remove contamination species, a wet-cleaning ultrasonic technique was applied. Firstly, the wafers were wiped twice with an acetone soaked tissue, normally used for cleaning optical equipment. Afterwards, the wafers were placed in the powersonic cleaning bath for 10 minutes in acetone at half power and room temperature. Then, the wafers were placed in the powersonic cleaning bath for 10 minutes in propan-2-ol at half power and room temperature in order to remove left-over acetone. Lastly, the wafers were spray-rinsed in propan-2-ol and blown dry by nitrogen gas. These diced wafers were used for further experiments, and stored individually in petri dishes throughout the experiment period.

6.4 Preparation of Silicon Dioxide Nanoparticles

Firstly, 5 mL of LUDOX® TM-40 colloidal silica was centrifuged at 10,000 RPM for 20 minutes in Greiner tubes. After centrifugation, remaining water was discarded, and the precipitated nanoparticles were dissolved in propan-2-ol, resulting in the stock SNP solution. Afterwards, the SNP stock solution was placed in the powersonic bath for 20 minutes and diluted 1:11. This SNP solution was applied during experiments and the OD_{600} values of SNP solutions were measured by the absorption spectrophotometer.
One drop of a SNP solution was suspended on three silicon dioxide wafers in order to perform size distribution measurements using AFM.
The size distribution measurements by the AFM were processed in Gwyiddion, using the watershed tool.

6.5 Fabrication of Superhydrophobic Surfaces

Firstly, three silicon dioxide wafers were placed in the ozone cleaner for 20 minutes. The topographies of the three wafers (untreated wafers) were measured by the AFM, in order to determine the RMS of the surfaces. Furthermore, the CAs were measured by a setup designed for the purpose using fresh milli-Q water. All CAs were measured in accordance with methods described by Stalder *et al.* [69].

In order to fabricate silicon dioxide wafers with a PFOTS monolayer, three silicon dioxide wafers were placed in the ozone cleaner for 20 minutes. Afterwards, CVD was performed in order to covalently link PFOTS to the silicon dioxide.
The topographies of the three wafers (PFOTS wafers) were measured by the AFM in order to determine the RMS of the surfaces. Lastly, CAs were measured.

In order to fabricate silicon dioxide wafers coated with SNPs, three silicon dioxide wafers were placed in the ozone cleaner for 20 minutes. Furthermore, the SNP solution was placed in the powersonic bath for 20 minutes and shaken before application. Afterwards, the SNP solution was dropped on the wafers, covering the entire wafer, which were then left for drying for 30 minutes. This step was done twice. The topographies of the three wafers (SNP wafers) were measured by the AFM in order to determine the RMS of the surfaces. In order to exclude large aggregates, potential contamination, and AFM artifacts during RMS calculation, a specific area of the topographies was selected, indicating representative RMS values. Lastly, the CAs were measured.

In order to fabricate the superhydrophobic surfaces, three silicon dioxide wafers were placed in the ozone cleaner for 20 minutes. Afterwards, the SNP solution was placed in a powersonic bath for 20 minutes and shaken before application. The SNP solution was dropped on the wafers, covering the entire wafer, which were then left for drying for 30 minutes. This step was done twice. Then CVD was performed in order to covalently link PFOTS to the SNPs.
The topographies of the three wafers (SNP-PFOTS wafers) were measured by the AFM in order to determine the RMS of the surfaces. In order to exclude large aggregates, potential contamination, and AFM artifacts during RMS calculation, a specific area of the topographies was selected indicating representative RMS values. Lastly, CAs were measured.

Lastly, six silicon dioxide wafers were placed in the ozone cleaner for 20 minutes. Furthermore, the SNP solution was placed in the powersonic bath for 20 minutes and shaken before application. Afterwards, the SNP solution was dropped on the wafers, covering the entire wafer, which were then left for drying for 30 minutes. This step was done twice. Then, the wafers were placed in the ozone cleaner again for 20 minutes in order to decompose potential organic agents of the SNP solution. The topographies of three irradiated wafers (SNP-UV wafers) were measured by the AFM in order to determine the RMS of the surfaces. In order to exclude large aggregates, potential contamination, and AFM artifacts during RMS calculation, a specific area of the topographies was selected indicating representative RMS values. Lastly, the CAs were measured.
By CVD, PFOTS was covalently linked to the SNPs of the three remaining wafers, forming a monolayer. The topographies of the three irradiated wafers (SNP-UV-PFOTS wafers) were measured by the AFM in order to determine the RMS of the surfaces. In order to exlude large aggregates, potential contamination, and AFM artifacts during RMS calculation, a specific area of the topographies was selected indicating representative RMS values. Lastly, the CAs were measured.

7. Results

7.1 Silicon Dioxide Nanoparticles

The SNP solution was prepared as described in Section 6.4. The concentration of SNPs in the stock SNP solution was unknown, however, the OD_{600} was determined for the stock SNP solution, a 1:11 dilution in propan-2-ol, and a 1:121 dilution in propan-2-ol, see Table 7.1.

Dilution	OD_{600}
Stock	1.516
1:11	0.161
1:121	0.003

Table 7.1: OD_{600} of the stock SNP solution, a 1:11 dilution in propan-2-ol, and a 1:121 dilution in propan-2-ol.

SNPs were suspended on wafers (a - c) in order to perform size distribution measurements by the AFM using semi-contact mode. See Figure 7.1 for AFM measurements. The AFM measurements were analysed in Gwyddion, resulting in histograms for wafers (a - c), visualizing counted particle diameters in bins of 15 nm. The wafers were prepared as described in Section 6.3.

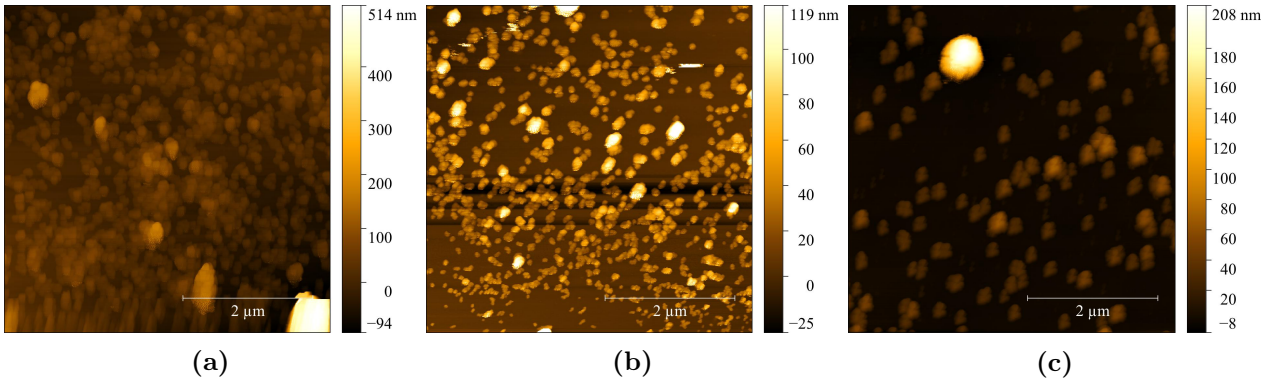

Figure 7.1: AFM measurements of wafers (a - c) performed on a 5 x 5 µm sample area using semi-contact mode. The dilution of the stock SNP solution was (a) 1:11, (b) 1:121, and (c) 1:121 respectively. AFM artifacts related to the tip is visible on wafer (c).

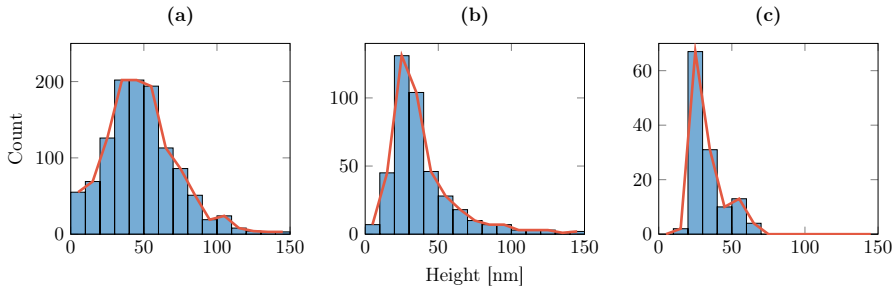

Figure 7.2: Histograms of wafers (a - c), visualizing counted particle diameters in bins of 15 nm. The red graph is a plot composed of the bin heights. The obtained mean diameters of SNPs were (a) 43.79 nm, (b) 36.41 nm, and (c) 33.52 nm, with highest count between (a) 30 - 60 nm, (b) 15 - 30 nm, and (c) 15 - 30 nm. The few particles or aggregates with diameters over 150 nm were left out.

7.2 Untreated Silicon Dioxide Wafers

The untreated wafers were prepared as described in Sections 6.3 and 6.5. AFM measurements were performed in semi-contact mode visualizing the topographies of the wafers, see Figure 7.3. The RMS values of the untreated wafers (d - f) were calculated from the AFM measurements. See Table 7.2 for RMS values and CAs for the untreated wafers (d - f).

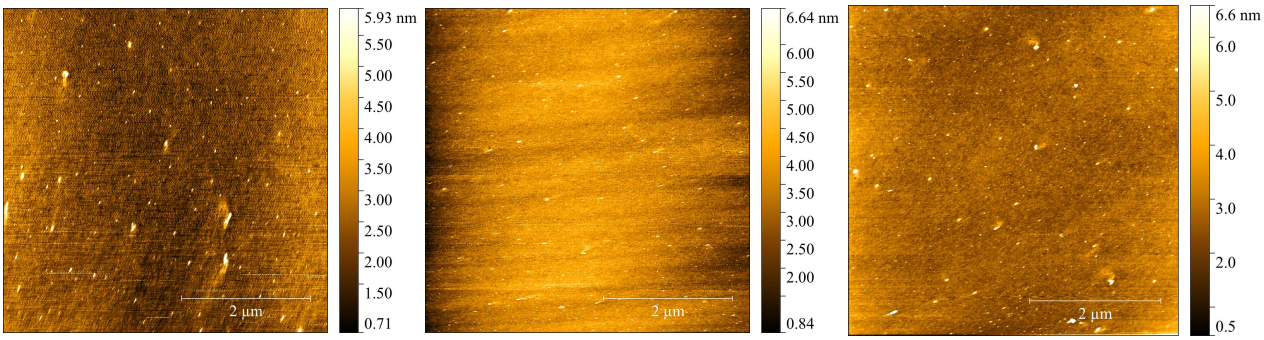

Figure 7.3: AFM measurements of untreated wafers (d - f) performed on a 5 x 5 µm sample area using semi-contact mode. RMS was calculated on the total 5 x 5 µm surface area. RMS was calculated to (d) 0.69 nm, (e) 0.76 nm, and (f) 0.69 nm. Contaminant particles with diameters below 5 nm were visible.

Corresponding CAs of the untreated wafers (d - f) were determined using a setup designed for the purpose, where a water droplet was suspended on the wafers. See Figure 7.4 for CA images. The CAs were measured using a CA plugin for ImageJ.

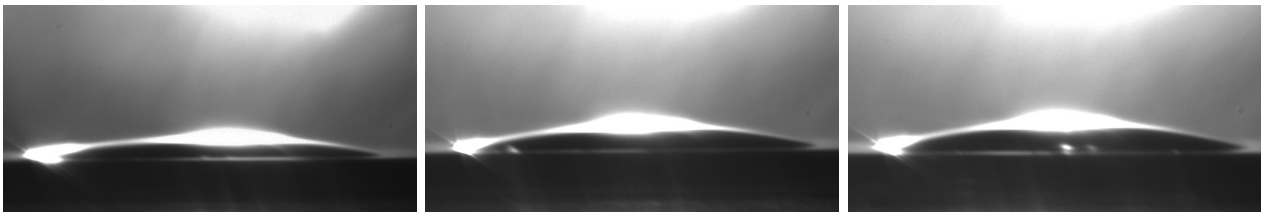

Figure 7.4: CA images of untreated wafers (d - f) with water. Contact angles were below 10°, rendering them unmeasurable.

Wafer	r	RMS [nm]	CA [°]
(d)	1.01	0.69	$< 10°$
(e)	1.01	0.76	$< 10°$
(f)	1.01	0.69	$< 10°$

Table 7.2: Roughness parameters r were obtained from the AFM measurements of untreated wafers (d - f), and utilized to calculate corresponding RMS values, see Equation (3.6). RMS values were calculated on the total 5 x 5 µm surface area. CAs of wafers (d - f) were below 10°, rendering them unmeasurable.

7.3 PFOTS Silicon Dioxide Wafers

The PFOTS wafers were prepared as described in Sections 6.3 and 6.5. AFM measurements were performed in semi-contact mode visualizing the topographies of the wafers, see Figure 7.5. The RMS values of the PFOTS wafers (g - i) were calculated from the AFM measurements. See Table 7.3 for RMS values and CAs for PFOTS wafers (g - i).

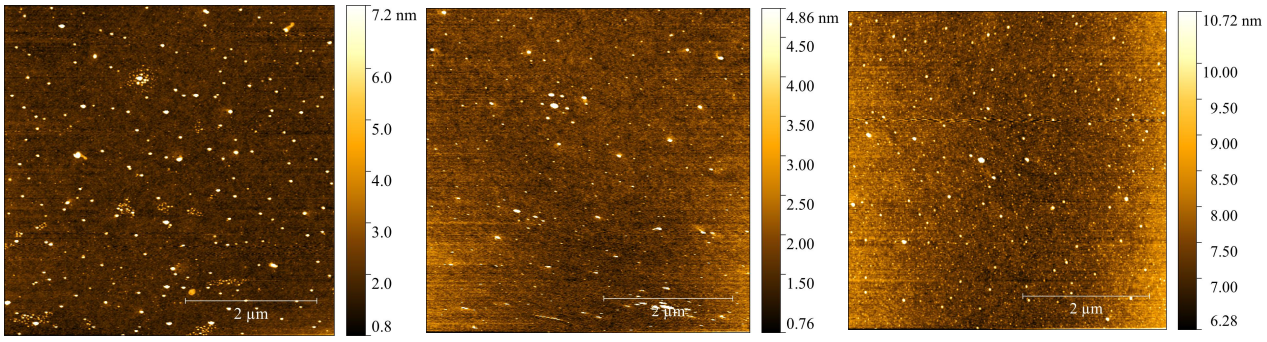

(g) **(h)** **(i)**

Figure 7.5: AFM measurements of PFOTS wafers (g - i) performed on a 5 x 5 µm sample area using semi-contact mode. RMS was calculated on the total 5 x 5 µm surface area. RMS values were calculated to be (g) 0.72 nm, (h) 0.52 nm, and (i) 0.57 nm. Contaminant particles with diameters below 5 nm were visible.

Corresponding CAs of the PFOTS wafers (g - i) were determined using a setup designed for the purpose, where a water droplet was suspended on the wafers. See Figure 7.6 for CA images. The CAs were measured using a CA plugin for ImageJ.

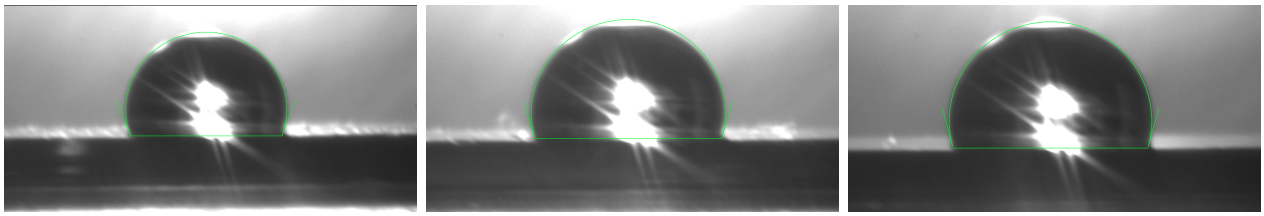

(g) **(h)** **(i)**

Figure 7.6: CA images of PFOTS wafers (g - i) with water. CAs were calculated to be (g) 111.53°, (h) 106.65°, and (i) 106.22°, using the green outline.

Wafer	r	RMS [nm]	CA [°]
(g)	1.00	0.72	111.53
(h)	1.00	0.52	106.65
(i)	1.00	0.57	106.22

Table 7.3: Roughness parameters r were obtained from the AFM measurements of PFOTS wafers (g - i), and utilized to calculate corresponding RMS values, see Equation (3.6). RMS values were calculated on the total 5 x 5 µm surface area.

7.4 SNP Silicon Dioxide Wafers

The SNP wafers were prepared as described in Sections 6.3 and 6.5. AFM measurements were performed in semi-contact mode visualizing the topographies of the wafers, see Figure 7.7. The RMS and RMS* values of the SNP wafers (j - l) were calculated from the AFM measurements. See Table 7.4 for RMS values and CAs of SNP wafers (j - l).

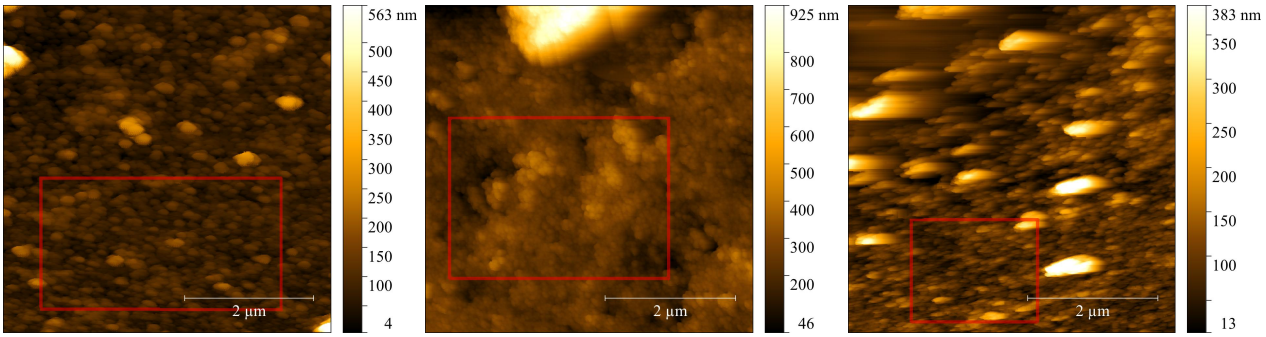

Figure 7.7: AFM measurements of SNP wafers (j - l) performed on a 5 x 5 µm sample area using semi-contact mode. RMS values were calculated on the total 5 x 5 µm surface area, where RMS* was calculated using the area defined by the red box. RMS values were calculated to be (j) 42.10 nm, (k) 111.00 nm, and (l) 31.50 nm. RMS* was calculated on areas (j) 7.86 µm^2, (k) 8.56 µm^2, and (l) 3.20 µm^2. The RMS* values were calculated to be (j) 26.20 nm, (k) 60.10 nm, and (l) 38.00 nm. The wafers were fully covered with SNPs.

Corresponding CAs of the SNP wafers (j - l) were determined using a setup designed for the purpose, where a water droplet was suspended on the wafers. See Figure 7.8 for CA images. The CAs were measured using a CA plugin for ImageJ.

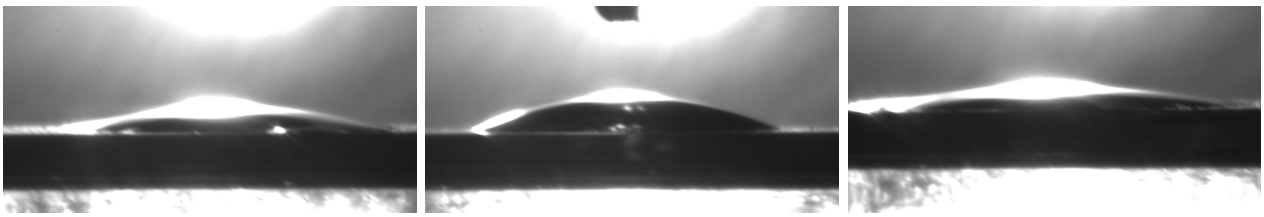

Figure 7.8: CA images of SNP wafers (j - l). CAs were below 10°, rendering them unmeasurable.

Wafer	r	RMS [nm]	RMS* [nm]	CA [°]
(j)	1.38	43.10	26.20	$< 10°$
(k)	1.36	111.00	60.10	$< 10°$
(l)	1.40	31.50	38.00	$< 10°$

Table 7.4: Roughness parameters r were obtained from the AFM measurements of SNP wafers (j - l), and utilized to calculate corresponding RMS and RMS* values, see Equation (3.6). RMS values were calculated on the total 5 x 5 µsurface area, where RMS* values were calculated on areas (j) 7.86 µm^2, (k) 8.56 µm^2, and (l) 3.20 µm^2. CAs of wafers (j - l) were below 10°, rendering them unmeasurable.

7.5 SNP-PFOTS Silicon Dioxide Wafers

The SNP-PFOTS wafers were prepared as described in Sections 6.3 and 6.5. AFM measurements were performed in semi-contact mode visualizing the topographies of the wafers, see Figure 7.9. The RMS and RMS* values of the SNP-PFOTS wafers (m - o) were calculated from the AFM measurements. See Table 7.5 for RMS values and CAs for SNP-PFOTS wafers (m - o).

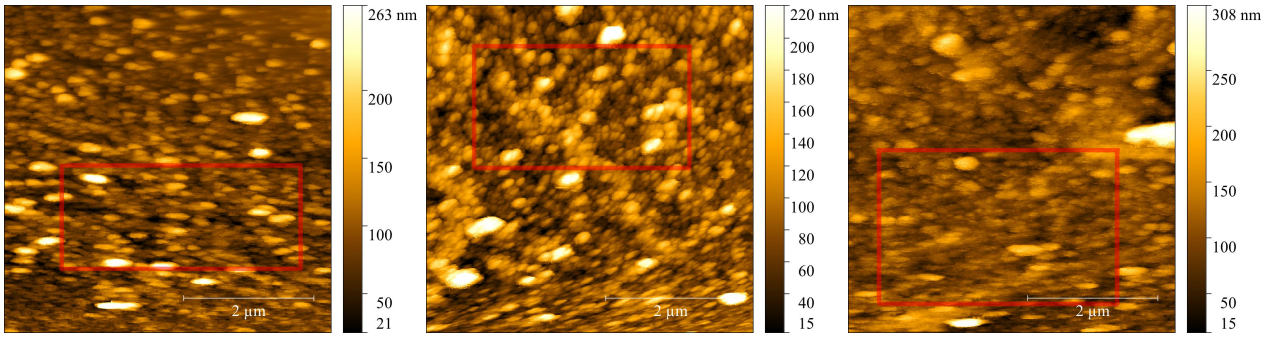

(m) **(n)** **(o)**

Figure 7.9: AFM measurements on SNP-PFOTS wafers (m - o) performed on a 5 x 5 µm sample area using semi-contact mode. RMS values were calculated on the total 5 x 5 µm surface area, where RMS* values were calculated using the area defined by the red box. RMS values were calculated to be (m) 31.50 nm, (n) 32.70 nm, and (o) 27.30 nm. RMS* values were calculated on areas (m) 6.18 µm^2, (n) 6.54 µm^2, and (o) 9.05 µm^2. The RMS* values were calculated to be (m) 36.20 nm, (n) 30.30 nm, and (o) 27.30 nm. The wafers were fully covered with SNPs.

Corresponding CAs of the SNP-PFOTS wafers (m - o) were determined using a setup designed for the purpose, where a water droplet was suspended on the wafers. See Figure 7.10 for CA images. The CAs were measured using a CA plugin for ImageJ.

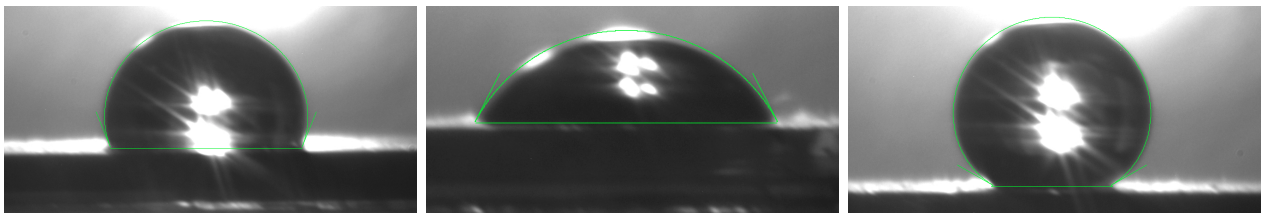

(m) **(n)** **(o)**

Figure 7.10: CA images of SNP-PFOTS wafers (m - o). CAs were calculated to be (m) 112.09°, (n) 62.37°, and (o) 150.44°, using the green outline.

Wafer	r	RMS [nm]	RMS* [nm]	CA [°]
(m)	1.41	31.50	36.20	112.09
(n)	1.32	32.70	30.30	62.37
(o)	1.46	27.30	27.30	150.44

Table 7.5: Roughness parameters r were obtained from the AFM measurements of SNP-PFOTS wafers (m - o), and utilized to calculate corresponding RMS and RMS* values, see Equation (3.6). RMS values were calculated on the total 5 x 5 µm surface area, where RMS* values were calculated on areas (m) 6.18 µm^2, (n) 6.54 µm^2, and (o) 9.05 µm^2. Wafers (m - o) had inconsistent CAs.

7.6 SNP-UV Silicon Dioxide Wafers

The SNP-UV wafers were prepared as described in Sections 6.3 and 6.5. AFM measurements were performed in semi-contact mode visualizing the topographies of the wafers, see Figure 7.11. The RMS and RMS* values of the SNP-UV wafers (p - r) were calculated from the AFM measurements. See Table 7.6 for RMS values and CAs for SNP-UV wafers (p - r).

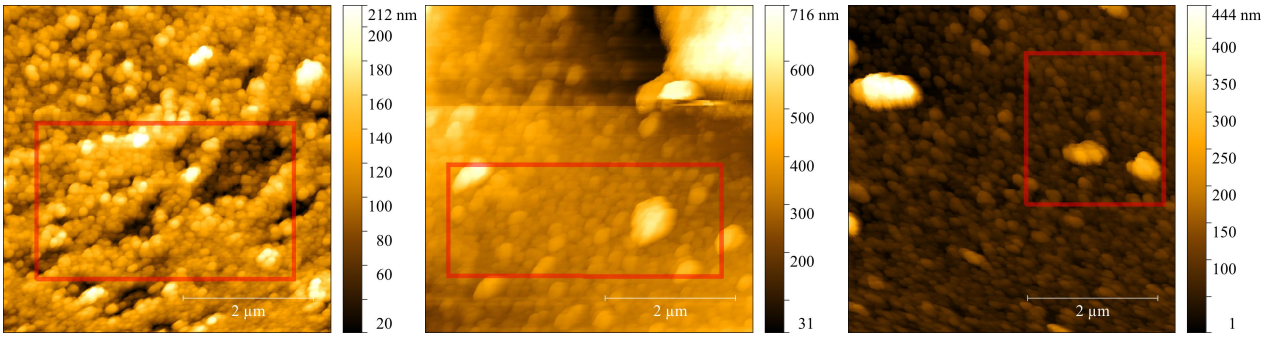

(p) **(q)** **(r)**

Figure 7.11: AFM measurements on SNP-UV wafers (p - r) performed on a 5 x 5 µm sample area using semi-contact mode. RMS values were calculated on the total 5 x 5 µm surface area, where RMS* values were calculated using the area defined by the red box. RMS values were calculated to be (p) 37.30 nm, (q) 109.10 nm, and (r) 47.90 nm. RMS* values were calculated on areas (p) 9.85 µm^2, (q) 7.56 µm^2, and (r) 5.21 µm^2. RMS* values were calculated to be (p) 30.50 nm, (q) 62.30 nm, and (r) 40.80 nm. The wafers were fully covered with SNPs.

Corresponding CAs of the SNP-UV wafers (p - r) were determined using a setup designed for the purpose, where a water droplet was suspended on the wafers. See Figure 7.12 for CA images. The CAs were measured using a CA plugin for ImageJ.

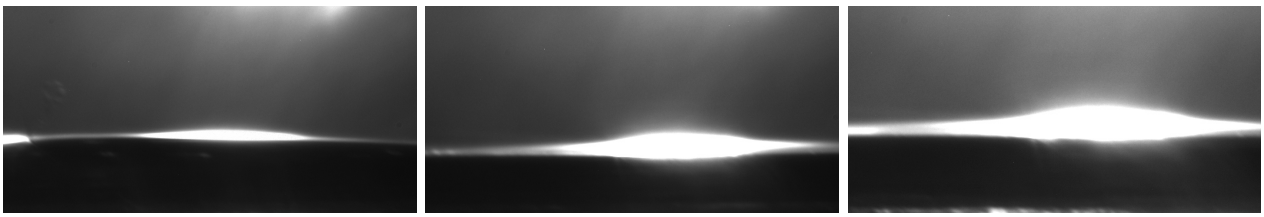

(p) **(q)** **(r)**

Figure 7.12: CA images of SNP-UV wafers (p - r) with water. CAs were below 10°, rendering them unmeasurable.

Wafer	r	RMS [nm]	RMS* [nm]	CA [°]
(p)	1.44	27.30	30.50	$< 10°$
(q)	1.23	109.10	62.30	$< 10°$
(r)	1.21	47.90	40.80	$< 10°$

Table 7.6: Roughness parameters r were obtained from the AFM measurements of SNP-UV wafers (p - r), and utilized to calculate corresponding RMS* and RMS values, see Equation (3.6). RMS values were calculated on the total 5 x 5 µm surface area, where RMS* values were calculated on areas (p) 9.85 µm^2, (q) 7.56 µm^2, and (r) 5.21 µm^2. CAs for SNP-UV wafers (p - r) were below 10°, rendering them unmesurable.

7.7 SNP-UV-PFOTS Silicon Dioxide Wafers

The SNP-UV-PFOTS wafers were prepared as described in Sections 6.3 and 6.5. AFM measurements were performed in semi-contact mode visualizing the topographies of the wafers, see Figure 7.13. The RMS and RMS* values of the SNP-UV-PFOTS wafers (s - u) were calculated from the AFM measurements. See Table 7.7 for RMS values and CAs for SNP-UV-PFOTS wafers (s - u).

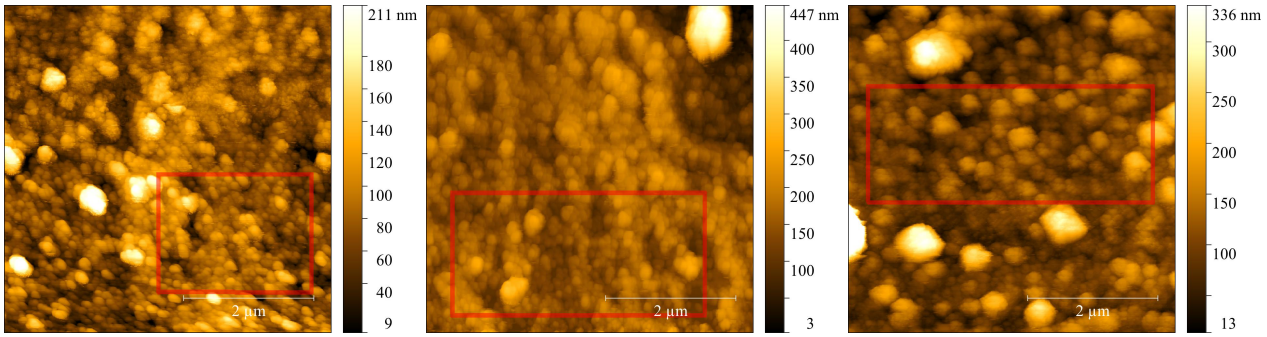

(s) **(t)** **(u)**

Figure 7.13: AFM measurements on SNP-UV-PFOTS wafers (s - u) performed on a 5 x 5 µm sample area using semi-contact mode. RMS values were calculated on the total 5 x 5 µm surface area, where RMS* values were calculated using the area defined by the red box. RMS values were calculated to (s) 29.90 nm, (t) 47.10 nm, and (u) 52.50 nm. RMS* values were calculated on areas (s) 4.53 µm^2, (t) 7.58 µm^2, and (u) 8.21 µm^2. The RMS* values were calculated to be (s) 24.40 nm, (t) 34.10 nm, and (u) 28.50 nm. The wafers were fully covered with SNPs.

Corresponding CAs of the SNP-UV-PFOTS wafers (s - u) were determined using a setup designed for the purpose, where a water droplet was suspended on the wafers. See Figure 7.14 for CA images. The CAs was measured using a CA plugin for ImageJ.

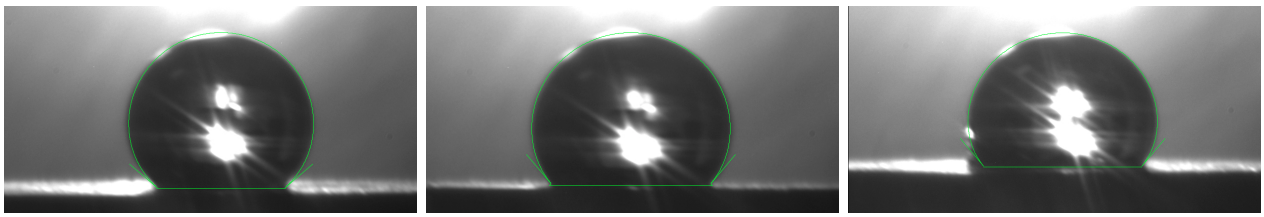

(s) **(t)** **(u)**

Figure 7.14: CA images of SNP-UV-PFOTS wafers (s - u). CAs were calculated to be (s) 129.29°, (t) 130.10°, and (u) 130.22°, using the green outline.

Wafer	r	RMS [nm]	RMS* [nm]	CA [°]
(s)	1.18	29.90	24.40	139.29
(t)	1.16	47.10	34.10	130.10
(u)	1.18	52.50	28.50	130.22

Table 7.7: Roughness parameters r were obtained from the AFM measurements of SNP-UV-PFOTS wafers (s - u), and utilized to calculate corresponding RMS and RMS* values, see Equation (3.6). RMS values were calculated on the total 5 x 5 µm surface area, where RMS* values were calculated on areas (s) 4.53 µm^2, (t) 7.58 µm^2, and (u) 8.21 µm^2.

8. Discussion

The size distribution measurements of the SNPs applied in this project, revealed mean particle diameters of (a) 43.79 nm, (b) 36.41 nm, and (c) 33.52 nm, with highest counts at (a) 30-60 nm, (b) 15-30 nm, and (c) 15-30 nm, see Figure 7.2. In the measurements, the baseline was chosen manually at the surface in order to exclude AFM artifacts, like shadows or drifting, as unrealistic baselines. On wafer (c), artifacts related to the tip was visible, See Figure 7.1, but the height profile of the measurements should not have been influenced.

It is evident that the mean diameters and the particle diameter with highest count are consistent on wafers (b) and (c), however, wafer (a) shows a mean particle diameter and a diameter of highest count that is roughly double those of wafers (b) and (c). The concentration of SNPs on wafer (a) (1:11) was higher than those of wafers (b) and (c) (1:121), and one could argue that the higher mean particle diameter of wafer (a) is a result of a higher concentration of SNPs as aggregates or stacked SNPs could potentially be included in the calculation of mean diameters. This is suspected since it is difficult to identify discrete particles and surface baseline on wafer (a).

W.R. Grace & Co.-Conn., who has LUDOX® trademarked, reports that the applied LUDOX® TM-40 SNP solution has an average particle diameter of 22 nm with a monodisperse size distribution [55, 56]. Furthermore, Lee *et al.* [70] have reported a measured mean particle diameter of 24.2 ± 2.7 nm of the LUDOX® TM-40 SNP solution, and Bravo *et al.* [7] reports a mean diameter of 20 nm. This is fairly consistent with measured mean particle diameters of wafers (a - c).

Nanoparticles can be applied in order to fabricate superhydrophobic surfaces, as they can contribute to surface roughness. However, one must choose an appropriate scale of roughness, and if the SNPs applied in this project are approximately 22 nm in diameter, they are potentially too small for fabrication of superhydrophobic surfaces. Bravo *et al.* [7] reported successful superhydrophobic surfaces with CAs above 150° and SAs below 5°, by utilizing layer-by-layer assembly resulting in a body layer of mixed 50 and 20 nm SNPs in polymers with three top layers of 20 nm SNPs in order to obtain two-scale roughness. Lastly, they coated the particle film with a PFOTS monolayer by CVD. Nimittrakoolchai *et al.* [3] reports successful superhydrophobic surfaces utilizing 40 - 45 nm SNPs deposited on etched substrates, followed by suspension of the substrates in a PFOTS solution. Wang *et al.* [12] reported successful superhydrophobic surfaces utilizing a sol-gel process, where the sol consisted of 50 - 100 nm SNPs and tridecafluorooctyl triethoxysilane. The sol solution was coated in a random fashion onto different substrates. Lastly, Kulkarni *et al.* [71] reported successful superhydrophobic surfaces by silanization of 100 - 150 nm SNPs, which was suspended on silicon dioxide substrates. These studies either utilize larger particles for one-scale roughness or the first layer of a two-scale roughness (50 nm [7], 50 - 100 nm [12], 100 - 150 nm [71]), or utilize similar or larger particles for the second layer of a two-scale roughness (20 nm [7], 40 - 45 nm [3]). Thus, one could argue that particles with a mean diameter of 22 nm are too small for one-scale roughness, as was attempted in this project. However, Ogihara *et al.* [72] reported successful superhydrophobic surfaces by spray-coating alcohol suspensions containing hydrophobic 25 nm SNPs on substrates. Thus it may be possible to continue fabricating superhydrophobic surfaces relying on 22 nm SNPs.

8.1 Experimental Considerations

The untreated wafers (d - f) were cleaned as described in Section 6.3 and dry-cleaned by the ozone cleaner. However, discrete particles with diameters below 5 nm are detectable in the AFM measurements of untreated wafers (d - f), see Figure 7.3. This indicates that the cleaning process applied in this project has not been sufficient. Cleaning of the wafers was performed ultrasonically in acetone and propan-2-ol. Ultrasonic cleaning was chosen due to even cleaning, originating from even distribution of cavitation collapse, and it is efficient at removing hydrophobic contaminants by cavitation and shock wave effects [60]. However, ultrasonic cleaning is efficient at removing particles larger than 300 nm, but requires a focused beam of high local intensity in order to effectively remove particles smaller than 100 nm in diameter [60]. Thus one could argue that the small contaminant particles on wafers (d - f) are too small to be removed by ultrasonic cavitation, and requires a higher energy to be dislodged or dispersed, or larger effects from shock waves available in megasonic systems [60].
Furthermore, it is important do apply proper cleaning chemicals when performing ultrasonic cleaning, where organic solvents can be utilized to dissolve organic contaminants leading to the dislodging and dispersion of contaminants [60]. Furthermore, many organic solvents are often mild cleaning chemicals compared to strong alkalines and acids, thus they do not induce unwanted substrate damage or dissolution. In this project, acetone was utilized as cleaning chemical as it efficiently dissolves organic compounds [60] and inorganic salts due to its polarity. However, acetone has a high vapour pressure and utilizing it risks redeposition of contaminant species. Thus, the cleaning process must be accompanied by post cleaning in stronger eluant solutions (e.g. propan-2-ol) [73, 74]. Furthermore, acetone has a very low flash point, thus acetone gas and liquid are very flammable, and it is generally advised not to use flammable solvents during ultrasonic cleaning, especially if elevated temperatures are used [75]. Generally, most organic solvents can be utilized as cleaning chemicals, and Baldacchini *et al.* [76] ultrasonically cleaned silicon wafers in trichloroethylene, acetone, and methanol, respectively, for 15 minutes. Nimittrakoolchai *et al.* [3] ultrasonically cleaned glass substrates in ethanol, acetone, and deionized water respectively.
However, the AFM measurements on untreated wafers (d - f) revealed RMS values of (d) 0.69 nm, (e) 0.76 nm, (f) 0.69 nm, see Table 7.2, while Meiners *et al.* [77] reported RMS values of 0.463 ± 0.029 nm on cleaned silicon dioxide wafers, and Kim *et al.* [4] reported RMS values of less than 0.6 nm on cleaned silicon dioxide wafers. Meiners *et al.* [77] prepared substrates by ultrasonic cleaning in toluene and propan-2-ol, respectively, for 5 minutes, followed by dry blowing in argon and ozone cleaning for 30 minutes. Kim *et al.* [4] do not report a cleaning method. Furthermore, the CAs of the untreated wafers (d - f) were unmeasurable as they were below 10°. This is consistent with Zafonte and Chiu [66] who report CAs after ultrasonic and ozone cleaning at 3 - 4°. It is evident that the cleaning process utilized in this project has left contaminant particles on the silicon dioxide wafers, however, the RMS values indicate that the wafers are approximately as clean as the cleaned silicon dioxide wafers used in the literature [4, 77].
It can be argued that the small contaminant particles may be inorganic. Firstly, since acetone and propan-2-ol are organic solvents, organic particles will have dissolved during ultrasonic cleaning. However, the organic particles may only be partially dissolved. Secondly, before application, every silicon dioxide wafer was ozone cleaned after ultrasonic cleaning, which should eliminate most organic contaminants by oxidation of organic compounds. Furthermore, it is suggested that the contaminant particles originates from preparation processes like dicing, where silicon dioxide particles and/or aggregates can have been dislodged or released from the wafers, followed by redeposition onto the surface. The contaminant particles may also originate from the deposition of photoresist, since the spin coater have multiple

purposes, and contaminant species from earlier applications may have deposited on the undiced silicon dioxide wafer. Furthermore, the contaminant particles may not originate from ultrasonic cleaning as redeposition was minimized by cleaning and rinsing in propan-2-ol, followed by blow drying by nitrogen gas [58, 60]. The effect of contaminant particles in further fabrication processes will be discussed.
The CAs of the untreated wafers (d - f) were unmeasurable, which corresponds with the fact, that silicon dioxide is a hydrophilic material [5]. The wafers (d - f) had small RMS values and it is not possible to deduce whether this small roughness had any influence on the CA.

As described in Chapter 7, PFOTS was used to coat wafers (g - i), (m - o), and (s - u) using CVD, and the coating correlates with a significant increase in CAs.
It was observed, that the untreated wafers (d - f) had CAs below 10°, while the CAs were (g) 111.53°, (h) 106.65°, and (i) 106.22° when untreated wafers were coated with a monolayer of PFOTS, see Table 7.3. This is in agreement with the fact, that the fluorinated end of PFOTS does not participate in hydrogen bonding with water, which induces a hydrophobic surface, ultimately increasing the CA. Using the methods (i.e. AFM and CA measurements) employed in this project, however, does not directly verify that there indeed is PFOTS present on the wafers, especially since PFOTS monolayers are virtually undetectable by the AFM. As can be seen in Figures 7.3 and 7.5, there is not much change between the AFM measurements before and after CVD, as is evident form the fact that the RMS values of the PFOTS wafers (g - i) and the untreated wafers (d - f) are nearly identical. This is supported by AFM images shown by Wang *et al.*, where differences between wafers coated with PFOTS and uncoated wafers are hard to spot [78]. There are many methods available, which would verify whether a monolayer of PFOTS was present on the wafers, as will be elaborated on in Section 8.2.
The CAs of the PFOTS wafers (g - i) were below the ones obtained by Tada *et al.* [79], who found that an organic silane, (heptadecafluorodecyl)trichlorosilane ($CF_3(CF_2)_7CH_2CH_2SiCl_3$), which is quite similar to PFOTS, induced CAs of 119.4 ± 0.7° on a flat substrate. It is even possible to argue, that the CAs measured in this project are slightly higher than they should be. The untreated wafers (d - f) should ideally have RMS values of 0 nm, instead of (d) 0.69 nm, (e) 0.76 nm, and (f) 0.69 nm. For the untreated wafers (d - f), this small roughness should decrease the CAs, as the surface becomes slightly more hydrophilic if a Wenzel state is assumed. It was not possible to measure the CAs on the untreated wafers however, and this theoretical decrease in CA was not possible to verify. On the other hand, the small RMS values would have increased the hydrophobic effect of the PFOTS wafers (g - i), but the change in CA would be very small, however, since the RMS values are below 1 nm. The aim of this project is to create superhydrophobic surfaces using SNPs and PFOTS, and unknown contaminants should therefore be a large problem for the conclusions of this project. The small nature of the RMS however, still makes it possible to detect a considerable difference in the CAs before and after treatment of both SNPs and PFOTS.
With smaller CAs of the PFOTS wafers (g - i) than expected, the process through which wafers are coated with PFOTS must be examined further. As mentioned, CVD was used to coat the wafers with a monolayer of PFOTS. During CVD, an incubation time of 45 minutes, at room temperature, in the presence of argon, was utilized, see Section 6.2. A study done by Bravo *et al.* [7], utilized a similar CVD technique, but had an incubation time of 1 hour. Baldacchini *et al.* [76] used an incubation time of 3 hours, in order to coat a rough wafer with a trichlorosilane. This could indicate that the incubation time of 45 minutes used in this project might be too short. Other techniques, beside CVD, are also used. Geer *et al.* [80] immersed the wafers in a 1 vol. % solution of PFOTS in anhydrous toluene for 5 minutes, before they rinsed the wafers twice with toluene followed by baking for 4 minutes at 120 °C. Banga *et al.* [81] immersed their wafers in a 1 mM PFOTS solution in toluene for various periods of

time and rinsed them in chloroform afterwards. The aforementioned methods are all two-step methods, that first makes the wafers rough, and then deposits the silane, including the method used in this project. A simplified fabrication process could be a one-step method. Ogihara *et al.* mixes SNPs with a solution containing a trichlorosilane, heats it and then deposits it on the substrate [72]. Kulkarni *et al.* fabricated SNPs, and then coated them by immersing the particles in a solution of a trichlorosilane in toluene. Afterwards, the coated particles were deposited on the substrates [71].
Too short incubation time could result in an incomplete formation of a full covering monolayer. According to Wang *et al.*, it is possible to verify, that a monolayer is covering the entire wafer using a combination of x-ray photoelectron spectroscopy and ion scattering spectroscopy [78]. Furthermore, methods, including weighing by a quartz crystal microbalance (QCM) weight, could be employed in order to determine the ideal incubation time for formation of a complete monolayer. This could be done by studying different incubation times and relying on the fact that when a complete monolayer is formed, no more organic silane will deposit on the substrate, thus no gain in weight will occur. Kurth *et al.* [82, 83] have used a QCM weight to verify the presence of a monolayer on a gold substrate, by weighing the substrate at different time intervals during the deposition process. Fourier transform spectroscopy attenuated total reflection (FTIR-ATR) could also be employed, using multiple reflections for higher sensitivity, to study if the amount of PFOTS on the wafer would increase if incubation times longer than 45 minutes were used [84].

With CAs of (g) 111.53°, (h) 106.65°, and (i) 106.22° for the PFOTS wafers, additional roughness is needed, in order to obtain a superhydrophobic surface with a CA above 150°. This was done by utilizing two layers of SNPs. The effect of an increase in roughness on the untreated wafers was first investigated. As is evident from a qualitative comparison between the CAs of untreated wafers (d - f) in Figure 7.4 and the CAs of SNP wafers (j - l) in Figure 7.8, there is no change in CA. This is contrary to what is expected if either a Cassie-Baxter or a Wenzel state is assumed. If a Cassie-Baxter state is assumed, an increase in roughness with no change in surface free energy would lead to an increase in CA. On the other hand, if a Wenzel state is assumed, an increase in roughness with no change in surface free energy should lead to a decrease in CA for hydrophilic surfaces. As is evident from the AFM measurements of wafers (j - l) and their corresponding RMS* values, the two layers of SNPs indeed induce a large increase in roughness. As no change in CA is observed a change in surface free energy could be the case. This could arise from different phenomena. Firstly, the SNP solution, which had been used prior to this project, could be contaminated with agents, that changed either the composition or energy of the surface. Secondly, the manufacturer, W.R. Grace & Co.-conn., write that they add antimicrobial agents to their LUDOX® solutions, and these agents could be responsible for the unexpected CAs [55].
After the roughness of the wafers was increased on SNP wafers (j - l), PFOTS was deposited using the same CVD procedure as for the PFOTS wafers (g - i). This should lead to an increase in CA, as it did between the untreated wafers and the PFOTS wafers. Again, there is consistently no visible change in the AFM measurements or RMS* values between SNP wafers (j - l) and the SNP-PFOTS wafers (m - o). But it is evident from a comparison between the CAs of SNP wafers (j - l), see Figure 7.8, and the CAs of SNP-PFOTS wafers (m - o), see Figure 7.10, that there is a large increase in CA after coating with PFOTS. However, the results are not consistent.
The CA of SNP-PFOTS wafers were (m) 112.09°, (n) 62.37°, and (o) 150.44°, see Figure 7.10. SNP-PFOTS wafer (m), shows a CA corresponding to a PFOTS wafer, which were 106.22 - 111.53°, see Figure 7.6. SNP-PFOTS wafer (n) shows a CA, which is between the one of an untreated wafer, see Figure 7.4, and the one for a PFOTS wafer, see Figure 7.6. Finally, SNP-PFOTS wafer (o) shows a

superhydrophobic CA, which indicates the right roughness, and that PFOTS has successfully formed a covering monolayer.
Since the CAs of SNP wafers (j - l) are consistent, aswell as the CAs of the PFOTS wafers (g - i), it can be argued that it is the deposition of PFOTS onto the SNPs that leads to the inconsistencies. As described above, the manufacturer had doped the applied SNP solution with antimicrobial agents, and the presence of those could very well influence the dynamics behind the formation of a PFOTS monolayer. These factors would result in inconsistent results, as is the case in this project.
In order to compensate for the inconsistency of the CAs of SNP-PFOTS wafers (m - o), the SNPs were irradiated in the ozone cleaner for 20 minutes after deposition on the wafers. It is probable, that the antimicrobial agents of the SNP solution are organic, thus they can be eliminated by employing the combination of gaseous ozone and UV radiation, ultimately oxidizing organic compounds. Firstly, SNP-UV wafers (p - r) were irradiated in the ozone cleaner after SNP deposition, and the surfaces were even more hydrophilic, see Figure 7.12, than those of untreated wafers (d - f), see Figure 7.4, and SNP wafers (j - l), see Figure 7.8. This indicates a Wenzel state, and the wafers (p - r) were too hydrophilic for any CA measurements to be made. This change in hydrophilicity occurs in spite of the fact that the RMS* values are consistent with the SNP wafers (j - l) and SNP-PFOTS wafers (m - o). Secondly, SNP-UV-PFOTS wafers (s - u) were irradiated in the ozone cleaner after SNP deposition and before PFOTS coating, and resulted in consistent CAs with similar RMS* values, compared to the SNP-PFOTS wafers (m - o) that had not been irradiated. The CAs of the SNP-UV-PFOTS wafers were (s) 139.29°, (t) 130.10°, and (u) 130.33°. It is evident that the SNP-UV-PFOTS wafers had consistent CAs, however, they are not, as intended, superhydrophobic.
One can argue, that irradiation by the ozone cleaner has reduced the inconsistency of the CAs, possibly by decomposing organic constituents in the SNP solution, including antimicrobial agents. As the surfaces are not superhydrophobic, even though a combination of roughness and low surface free energy has been applied, it was discussed whether potential stabilizers of the SNP solution could influence the deposition of the PFOTS monolayer, potentially disrupting the superhydrophobic effect. However, it was obtained from W.R. Grace & Co.-conn. that every grade of the LUDOX® family is charge stabilized in order to keep the reactive SNPs from aggregating and gelling [56]. Specifically, the applied LUDOX® TM-40 SNP solution was stabilized by sodium hydroxide, resulting in an alkaline solution and negatively charged SNPs [56]. The stabilization relies on the silanol groups on the surface of the SNPs, where sodium hydroxide induces a negative charge with sodium as the counter ion, which balances the induced charge of SNPs [56]. W.R. Grace & Co.-conn. reports that the sodium counter ions remain in coatings with the SNPs after application and drying [56]. The sodium ions will not be influenced by the ozone cleaning processes, and thus one could argue that these ions may cause problems during CVD and the formation of the PFOTS monolayer. However, W.R. Grace & Co.-conn. reports that it is a small amount of the particle surface that is modified and that the reactivity of the SNPs primarily relies on that of the silica surface. Thus, effects from sodium ions are minimal. The problems arising from pre-fabricated SNPs could have been avoided by self-synthesizing the particles without any stabilizers or other unwanted components.
Another explanation as to why the SNP-UV-PFOTS wafers were not superhydrophobic, may be found in the size of the applied SNPs. The SNPs had a mean diameter of 22 nm, and, as described earlier in this chapter, it is popular to utilize either larger nanoparticles for one-scale roughness, or similar or larger particles for the second layer of a two-scale roughness. Thus, the 22 nm particles may be too small for one-scale roughness, and even though low surface free energy is utilized through coating, the roughness was not sufficient for superhydrophobic surfaces, not including the SNP-PFOTS wafer (o) as wafers (m - o) were inconsistent. However, by utilizing two-scale roughness with the 22 nm

SNPs as the primary layer, and smaller particles as the secondary layer, the 22 nm SNPs may induce superhydrophobicity, similar to what was reported by Bravo *et al.* [7] who utilized 20 nm and 7 nm particles. Furthermore, according to Bravo *et al.* [7], in order to obtain a Cassie-Baxter, and not a Wenzel state, two-scale roughness is essential for fabrication of ideal superhydrophobic surfaces, with a CA above 150° and a CAH below 10°. Furthermore, it may be required that the first layer of the two-scale roughness consists of a mixture of different sized nanoparticles in order to obtain a low CAH. [7]

Lastly, it is important to note, that no efforts were made to determine whether the wafers were entirely covered with a relatively homogeneous coating of SNPs and PFOTS. The solution of SNPs suspended in propan-2-ol was dispersed over the entire wafer, but the dynamics behind the evaporation of the propan-2-ol is not known, and were not investigated. In further studies, AFM images of different areas on each wafer could be employed to effectively determine the presence of a coating on the entire wafer. If the coating of SNPs and PFOTS was not relatively homogeneous, the CAs might depend on the placement of the droplet on the wafers. The RMS values, determined from all the AFM images presented in Chapter 7, were not deemed representative of all wafers due to random aggregates of particles and AFM artifacts. Some wafers showed aggregates in the AFM images, where others did not, and so, the determined RMS values were inconsistent. The aggregation was most likely due to the fact that the SNPs were suspended in propan-2-ol in between the experiments. Ogihara *et al.* showed that SNPs suspended in lower alchohols would aggregate more than if they were suspended in higher alcohols [72]. Propan-2-ol is an alchohol with a relatively high polarity [85], and thus, SNPs would aggregate more when in this solution compared to higher alcohols. Efforts were made to prevent this phenomenon from affecting the results using ultrasound for 20 minutes. It is not known, however, if 20 minutes was enough time to dissolve all aggregates, as their existence and size on the wafers seemed, as stated earlier, somewhat random. In future experiments, efforts should be made to minimize this effect further so that more consistent AFM results are obtained. As the RMS values were fairly inconsistent, RMS* values were used instead as these show a more representative value of the wafers. The RMS* values were found using smaller areas of the same AFM image. These areas were made as large as possible to ensure the RMS* values were statistically valid, while avoiding aggregates and AFM artifacts.

As stated in Section 3.2, the roughness parameter r should be proportional to the RMS value of a wafer, but that is not the case in this project. As is evident from every RMS value of untreated wafers (d - f) and PFOTS wafers (g - i), see Tables 7.2 and 7.3, and every RMS* value determined in this project, see Tables 7.4, 7.5, 7.6, and 7.7, there is no observable proportional correlation between r and these values of the AFM measurements. This means, that even after choosing an assumed representative area of the AFM image, there are considerable uncertainties in the determination of both the r and the RMS* value. Many studies report using AFM measurements for calculation of RMS values of their wafers, and use these in their assessments of the experiments. Therefore, AFM is clearly an accepted method for the determination of the RMS* values [7, 3, 86]. Others, however, use field emission scanning electron microscopy [4, 6] and transmission electron microscopy [71]. As AFM is a popular method of determining the roughness of a substrate, the measurements made in this project needs to be examined further, as the measurements are inconsistent with theory. Firstly, as can be seen in Figures 7.7 (k), 7.7 (l), 7.9 (m - o), and 7.11 (q), 7.11 (r), and 7.13 (t), there are significant drift, blurriness, and other AFM artifacts on these AFM images. These AFM artifacts can arise from too low feedback gain, too fast scanning speeds, and thermal and sample drift. Low feedback gain and too fast scanning speeds would result in a higher apparent RMS value, and so would thermal drift, since it stretches the particles in the plane of the substrate. However, most AFM artifacts have been avoided by selecting a specific area for RMS value calculation.

The CAs in this project, were measured using ImageJ, as stated in Chapter 6. This analysis tool, however, has some subjective aspects to it, and one example is the shape of the droplet. The shape of the water droplet was adjusted, and afterwards optimized using an algorithm. The primary determination of the shape, however, is made by the authors, and therein lies a potential source of error. Small variations in the determined shape can lead to a change of several degrees in the CA. The primary reason as to why the authors had to manually adjust the shape of the droplet was due to the low quality of the images. It would therefore be optimal if a higher resolution camera was utilized, such that images of higher quality would make it possible for an algorithm to completely determine a more accurate shape of the droplet, and thus eliminate this potential source of error.
Another consideration related to the measurement of the CAs is how the droplet was deposited on the wafers. The equipment made it impossible to keep the volume of the droplet constant throughout the experiments. There have been much research on how the volume of the droplet changes its CA, and Delich *et al.* have concluded, that on an ideal flat surface, the volume does not matter much [87]. However, when the CAH plays a role in the experiments, it has been shown that the volume of the droplet indeed is important [88]. If further research is to be conducted, a constant, fixed volume must be applied. When a droplet was formed on the wafers, the needle was inside the droplet. Fluid was supplied using a syringe with Milli-Q water connected to a tube. When the droplet had an appropriate size, the flow of water was stopped, but a smaller amount of liquid continued to flow, and so the syringe had to be retracted a bit to stop this flow. Some times this could result in some fluid flowing backwards into the tube from the droplet, and other times the reverse was the case. This can have a large effect on the CA of the droplet, due to CAH. If any liquid was removed from the droplet, the CA, rather than the contact area with the wafer, would decrease. If any liquid was added to the droplet, however, the CA would increase. CAH measurements were not conducted in this report, and so it is not evident how much of an effect this source of error has, but it has the potential to distort the results.

8.2 Improvements

As mentioned earlier, a method that verifies that the CVD process indeed resulted in a PFOTS monolayer covering the entire wafer should have been employed in this project. FTIR-ATR would have been an obvious choice, and the method is often used to characterise monolayers on a substrate [84, 71, 89, 90]. Fourier transform spectroscopy (FTIR) is a form of infrared (IR) spectroscopy, that makes it possible to measure the IR absorption of a continuous spectrum of wavenumbers almost instantaneously with a low signal-to-noise ratio [91, 92, 93]. The name stems from the fact that the method utilizes Fourier transformation. A specific form of FTIR is attenuated total reflection (ATR), which utilizes a crystal with total internal reflection, that is in contact with the sample. The light hits the sample, where some energy is absorbed by the sample, and the reflected light, which afterwards hits the detector, can thus yield information about the monolayer [84, 94]. Ha *et al.* studied PFOTS in collapsed form, on a zinc-selenide substrate and on a gold evaporated glass substrate using FTIR-ATR, see Figure 8.1a [95].

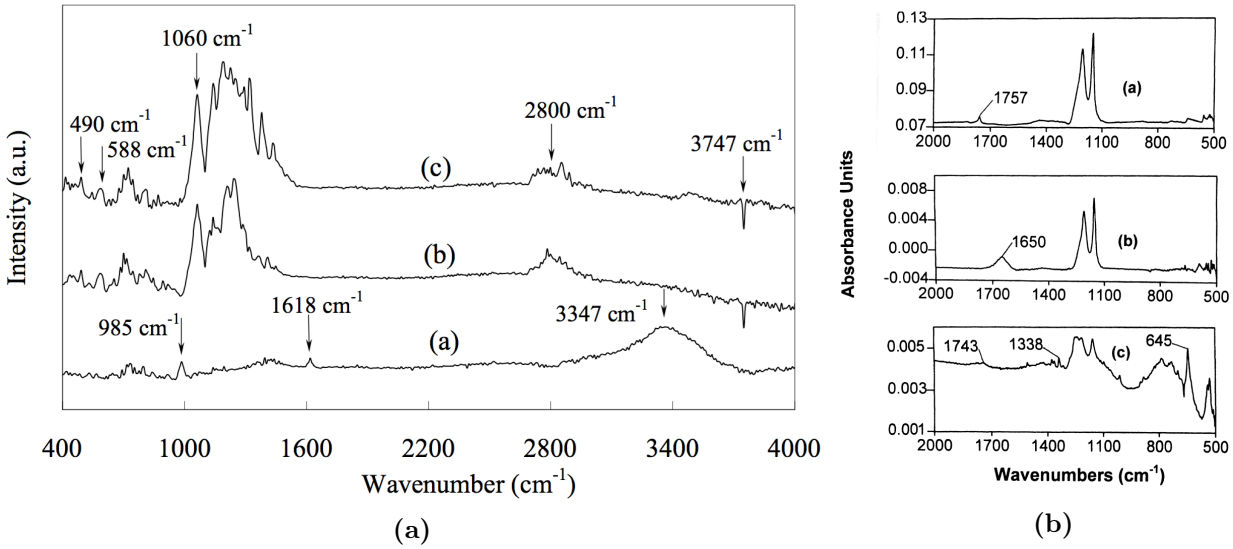

Figure 8.1: (a): FTIR-ATR spectra of PFOTS on a zinc-selenide substrate and on a gold evaporated glass substrate. There are two peaks of absorption, one at 1208 and one at 1152 cm^{-1}. These two peaks are attributed to the vibrational stretching of the C−F bond in the CF_2 and CF_3 groups [95]. (b): FTIR-ATR spectra of PFOTS deposited on a hydrated silica substrate at high temperatures. The peaks from 1450 to 700 cm^{-1} were attributed to the various C−H and C−F bonds [96].

In Figure 8.1a, it can be clearly seen, that there are two peaks of absorption, one at 1208 and one at 1152 cm^{-1}. These two peaks are attributed to the vibrational stretching of the C−F bond in the CF_2 and CF_3 groups [95].
Chen *et al.* used FTIR-ATR to explore how PFOTS was deposited on a hydrated silica substrate at high temperatures [96]. In Figure 8.1b, it is spectrum (b), which shows the absorption spectrum of PFOTS on the substrate, and the peaks from 1450 to 700 cm^{-1} were attributed to the various C−H and C−F bonds [96]. In studies by Fernández *et al.*, they found the anti symmetrical vibrational stretching of the CF_3 group in a CF_3SO_2X molecule to be in the range from 1190 to 1235 cm^{-1} [97, 98]. As is clear, FTIR-ATR could have easily been employed in this project to verify the presence of PFOTS on the silicon dioxide wafers.
Another measurement method, which is widely used to characterize monolayers, is spectroscopic ellipsometry (SE) [99, 100]. Ellipsometry measures the change in polarization of a light wave, that is either reflected from, or transmitted through a sample. It is then possible to gain insight into the thickness and optical properties of a thin film such as a monolayer. [99, 100]
In this project, SE would have been useful when characterizing the PFOTS monolayer as it could be determined if the measured thickness was consistent with the theoretical height of a PFOTS monolayer. DePalma *et al.* found the height of PFOTS to be approximately 10 Å using SE, which they reported to be in accordance with theoretical values [101].

Another addition to this project would be the examination of SAs and CAH. As stated earlier in Section 3.3, much literature conclude that a droplet in the Wenzel state will have a high SA and CAH, while a droplet in the Cassie-Baxter state will have a low SA and CAH [5, 45, 46]. Measurements of these two parameters would have helped elucidate which state the droplets in this project were in. Furthermore, SAs are a critical aspect of superhydrophobicity, since self-cleaning is a trait, that is highly sought after. For a surface to be self-cleaning, like the sacred lotus leaves, it must have a low SA and CAH, so any droplets will roll of easily, and collect any contaminants on the way as explained in Section 3.3. The stability of a surface structure is important for any practical use of a superhydrophobic surface,

and the stability of the coatings of the wafers created in this project was not investigated. Kim *et al.* made superhydrophobic surfaces that were stable for 30 days at both room temperature and up to 400 °C in atmospheric air [6]. According to Latthe *et al.* [102], superhydrophobic surfaces has been made, that were stable at temperatures up to 275 °C in high humidity. Another superhydrophobic surface was stable in toluene for 24 hours at room temperature, which is reported to indicate a stability in most organic solvents [103]. Other studies have reported their superhydrophobic surface to be stable in seawater even after long durations of exposure [104, 105, 106, 107, 108]. Lastly, another superhydrophobic surface was stable in pH values of 1 - 14, indicating that the pH value of an aqueous solution has little effect on the hydrophobicity of a surface [109]. These studies indicate that superhydrophobic coatings can be applied in a wide variety of environments. However, the stability of the specific coating made in this project is yet to be tested.

In order to manufacture a superhydrophobic surface, various methods can be used. For all methods, however, it is the combination of a low surface free energy and a rough surface that causes the superhydrophobicity. In this project, SNPs were deposited onto a surface in order to enhance roughness of the surface, followed by a coating of silane by CVD in order to lower the surface free energy.
For large-scale production, a one-step method may be beneficial, compared to the two-step method used in this project, due to the increased simplicity in both process and equipment. Wang *et al.* [12] used a one-step method to create a superhydrophobic surface. A sol solution containing SNPs was prepared by co-hydrolysis and condensation of two silane precursors, tetraethyl orthosilicate and tridecaflourooctyl triethoxysilane, in a hydrous ammonium solution. This solution can easily be coated onto various substrates simply by dipping, spraying, or spin coating, where it will form a transparent film. Once coated onto the surface, SNPs with a size range of 50 – 150 nm covered in silane species will randomly form aggregates. This will ensure both a low surface free energy and a high roughness, creating the premise of a superhydrophobic surface. Using this method on a polyester surface, a CA and SA of 174 ± 2.7° and 2.2 ± 0.1°, respectively, was achieved. [12]
The production method used by Wang *et al.*, compared to the method used in this project, is especially advantageous in a large-scale production. The production method is quite simple, as it is a one-step method and the coating process does not demand much in either process or equipment. The sol solution can easily be coated onto larger surfaces and the coating time is essentially independent of the surface area. Furthermore, the sol solution can be coated onto a wide array of solid surfaces, including textile fabrics, electrospun nanofibre mats, filter paper, glass slides, and silicon wafers [12]. Since the solution will form a transparent film once coated onto a surface, it is ideal for surfaces such as windows, car windshields, or clothes in order to make them self-cleaning.
Instead of only using nanoparticles for roughness, Baldacchini *et al.* used a femtolaser to create a microstructure which was efficient at trapping air beneath the water droplets, creating a Cassie-Baxter state on the surface [76]. The advantages of the femtolaser include the possibility to precisely modify the surface, rather than relying on the somewhat random nature of the deposition method used in this project. The femtolaser microtexturing would be useful for more precise experiments relating the roughness to the hydrophobicity of a surface. However, from an industrial perspective, femtolaser microtexturing might have some disadvantages. Baldacchini *et al.* uses a femtolaser with 1 kHz pulses with a spotsize of maximum 250 µm in diameter and then translates the surface relative to the laser spot in order to transform the entire surface [76]. Every spot on the surface receives an average of 200 pulses [76]. Thus, it would take 8 seconds to transform a 1 cm line of width 250 µm on the surface. In order to create 1 cm^2 transformed surface, 40 lines of 1 cm length would be needed, meaning 1 cm^2 would take 320 seconds to transform. From this estimation, it can be seen that the technology would

probably not scale too well with increasing surface area.
Etching is another possibility for creating appropriate roughness without relying on complex methods. Qian *et al.* [110] utilizes dislocation-selective chemical etching on aluminium, copper, and zinc surfaces to successfully create superhydrophobic surfaces with a CA of around 150° and a CAH around 5°, see Figure 8.3. The chemical etchant targets dislocation defects in crystalline materials, which are more prone to being dissolved than the crystalline material itself, due to the defects possessing relatively higher energy [110]. After the chemical etching, the surfaces were coated with a fluoroalkylsilane to make the surface hydrophobic. This method is quite simple to employ as roughness changes with the amount of time the surface is exposed to the dislocation etchant. The etching process should also be easier to scale up compared to the femtolaser microtexturing. Sarkar *et al.* exposed aluminium surfaces to diluted hydrochloric acid and afterwards coated them in Teflon® obtaining a CA of 164 ± 3° with a CAH of 2.5 ± 1.5° [111]. This method is also relatively simple compared to the femtolaser microtexturing, as only common industrial processes are used.
Furthermore, a surface with a very high roughness can also be achieved by creating a fractal surface, which was shown by Onda *et al.* [13]. For a fractal surface, the roughness parameter r, given by Equation (3.6), is very large and can even be infinite for a mathematical ideal fractal surface. In order to create the fractal surface, alkylketene dimer (AKD) solid films were grown with a thickness of 100 µm on a glass substrate. The glass substrate was dipped into melted AKD at 90 °C and was then cooled to room temperature in the ambience of dry nitrogen gas. When AKD solidifies it undergoes a fractal growth, resulting in a fractal surface. For this surface a CA as large as 174° was achieved, whereas for a flat AKD surface a CA of only 109° was achieved. Just as with the sol-gel method used by Wang *et al.*, the growth of AKD solid films, creating a fractal surface, could easily by applicable in a large-scale production and on large surfaces, as one would only need to dip the surface in melted AKD and then let it dry in order to achieve a superhydrophobic surface. A SEM image of the fractal surface is shown in Figure 8.2. [13]

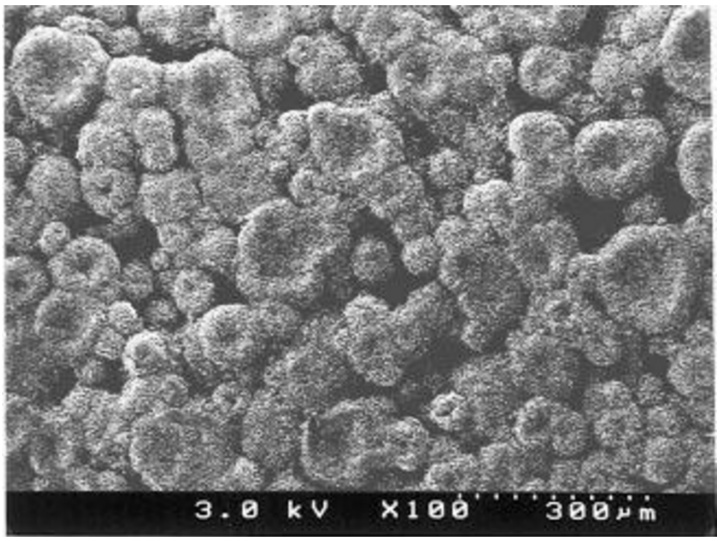

Figure 8.2: SEM image of fractal roughness created with AKD solid films with a thickness of 100 µm [13].

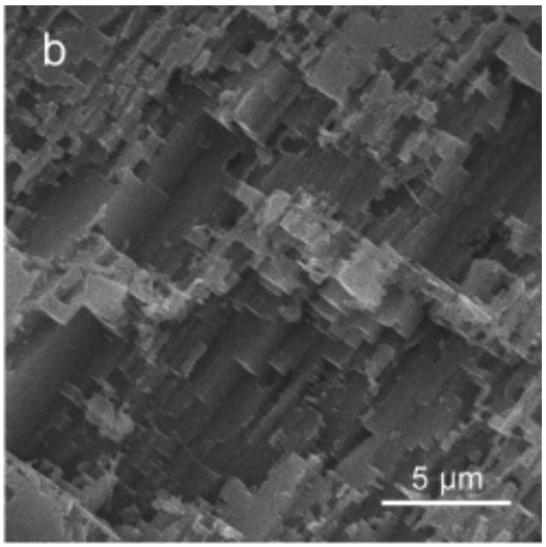

Figure 8.3: SEM image of an aluminum surface etched with a dislocation etchant for 10 seconds. The surface is afterwards coated with flouroalkylsilane to provide CAs around 150°. [110]

9. Conclusion

This project sought out to create superhydrophobic surfaces using a combination of two layers of SNPs and a coating of PFOTS. The two layers of SNPs were deposited in order to make a rough surface, and PFOTS was used to lower the surface free energy of the surfaces, as the theory behind superhydrophobic surfaces states that these are the two most important parameters.
More hydrophilic surfaces were obtained when coating with only SNPs, and more hydrophobic surfaces were obtained when coating with only PFOTS, compared to the untreated wafers. After a process of trial and error, surfaces that had been cleaned, exposed to UV radiation, coated with two layers of SNPs, once again exposed to UV radiation, and lastly coated with PFOTS using CVD, had CAs between 130 and 139°. Among the possible reasons why the surfaces had CAs below 150° could be the lack of two-scale roughness, and appropriate size of particles. Furthermore, it was not verified whether the entirety of the wafer surfaces was covered with PFOTS and SNPs or not.
There are several improvements that could be made to the experiments done in this project, if further research is to be conducted. First and foremost, either QCM weighing or FTIR-ATR should be used to determine whether there indeed was a monolayer of PFOTS formed on the wafers, that completely covered the entire wafer surface. Secondly, SA and CAH measurements should be done as to further determine whether the droplet is in a Wenzel or Cassie-Baxter state, and to check if the experiments have yielded an ideal superhydrophobic surface that can be used in various applications. Thirdly, one-step methods could be more attractive, compared to the two-step method applied in this project.

Bibliography

[1] Minglin Ma and Randal M Hill. Superhydrophobic surfaces. *Current opinion in colloid & interface science*, 11(4):193–202, 2006.

[2] Hans J Ensikat, Petra Ditsche-Kuru, Christoph Neinhuis, and Wilhelm Barthlott. Superhydrophobicity in perfection: the outstanding properties of the lotus leaf. *Beilstein journal of nanotechnology*, 2(1):152–161, 2011.

[3] On-Uma Nimittrakoolchai and Sitthisuntorn Supothina. Deposition of organic-based superhydrophobic films for anti-adhesion and self-cleaning applications. *Journal of the European Ceramic Society*, 28(5):947–952, 2008.

[4] Eun-Kyeong Kim, Chul-Sung Lee, and Sang Sub Kim. Superhydrophobicity of electrospray-synthesized fluorinated silica layers. *Journal of colloid and interface science*, 368(1):599–602, 2012.

[5] Yonghao Xiu. *Fabrication of surface micro-and nanostructures for superhydrophobic surfaces in electric and electronic applications*. ProQuest, 2008.

[6] Eun-Kyeong Kim, Ji Yeong Kim, and Sang Sub Kim. Synthesis of superhydrophobic sio 2 layers via combination of surface roughness and fluorination. *Journal of Solid State Chemistry*, 197:23–28, 2013.

[7] Javier Bravo, Lei Zhai, Zhizhong Wu, Robert E Cohen, and Michael F Rubner. Transparent superhydrophobic films based on silica nanoparticles. *Langmuir*, 23(13):7293–7298, 2007.

[8] Laurence W McKeen. *The effect of temperature and other factors on plastics and elastomers*. William Andrew, 2014.

[9] Scott Jenkins. Nanoiengineering infuses growing coatings market. *Chemical Engineering*, 120(4):17 – 22, 2013.

[10] Zhiqing Yuan, Hong Chen, Jide Zhang, Dejian Zhao, Yuejun Liu, Xiaoyuan Zhou, Song Li, Pu Shi, Jianxin Tang, and Xin Chen. Preparation and characterization of self-cleaning stable superhydrophobic linear low-density polyethylene. *Science and Technology of Advanced Materials*, 9(4):045007, 2008.

[11] Changhong Su, Jun Li, Hongbin Geng, Qingjun Wang, and Qingmin Chen. Fabrication of an optically transparent super-hydrophobic surface via embedding nano-silica. *Applied Surface Science*, 253(5):2633–2636, 2006.

[12] Hongxia Wang, Jian Fang, Tong Cheng, Jie Ding, Liangti Qu, Liming Dai, Xungai Wang, and Tong Lin. One-step coating of fluoro-containing silica nanoparticles for universal generation of surface superhydrophobicity. *Chemical communications*, (7):877–879, 2008.

[13] Tomohiro Onda, Satoshi Shibuichi, Naoki Satoh, and Kaoru Tsujii. Super-water-repellent fractal surfaces. *Langmuir*, 12(9):2125–2127, 1996.

[14] Lidiya Mishchenko, Benjamin Hatton, Vaibhav Bahadur, J. Ashley Taylor, Tom Krupenkin, and Joanna Aizenberg. Design of ice-free nanostructured surfaces based on repulsion of impacting water droplets. *ACS Nano*, 4(12):7699 – 7707, 2010.

[15] Michael Nosonovsky and Vahid Hejazi. Why superhydrophobic surfaces are not always icephobic. *ACS Nano*, 6(10):8488 – 8491, 2012.

[16] Ka Lum, David Chandler, and John D Weeks. Hydrophobicity at small and large length scales. *The Journal of Physical Chemistry B*, 103(22):4570–4577, 1999.

[17] Frederick M. Fowkes. Attractive forces at interfaces. *Industrial & Engineering Chemistry*, 1964.

[18] KL Johnson, K Kendall, and AD Roberts. Surface energy and the contact of elastic solids. In *Proceedings of the Royal Society of London A: Mathematical, Physical and Engineering Sciences*, volume 324, pages 301–313. The Royal Society, 1971.

[19] Frank Albert Cotton, Geoffrey Wilkinson, and Paul L Gaus. Basic inorganic chemistry. 1976.

[20] Da-Wen Sun. *Emerging technologies for food processing*. Elsevier, 2014.

[21] Peter Atkins and Julio de Paula. *Physical Chemistry*. Oxford Universty Press, 2014.

[22] SK Bhasin. *Pharmaceutical Physical Chemistry: Theory and Practices*. Pearson Education India, 2012.

[23] P Roura and Joaquim Fort. Local thermodynamic derivation of young's equation. *Journal of colloid and interface science*, 272(2):420–429, 2004.

[24] Lin Feng, Shuhong Li, Yingshun Li, Huanjun Li, Lingjuan Zhang, Jin Zhai, Yanlin Song, Biqian Liu, Lei Jiang, and Daoben Zhu. Super-hydrophobic surfaces: from natural to artificial. *Advanced materials*, 14(24):1857–1860, 2002.

[25] Yuehua Yuan and T. Randall Lee. Contact angle and wetting properties. *Springer Series in Surface Sciences*, 2013.

[26] X Li, D Reinhoudt, and M Crego-Calama. What do we need for a superhydrophobic surface? a review on the recent progress in the preparation of superhydrophobic surfaces. *The Royal Society of Chemistry*, 2007.

[27] AW Adamson. Physical chemistry of surfaces (5th edn.) interscience. *New York*, 1990.

[28] Yixiong Liu and RM German. Contact angle and solid-liquid-vapor equilibrium. *Acta materialia*, 44(4):1657–1663, 1996.

[29] Gerald H Meier. *Thermodynamics of Surfaces and Interfaces: Concepts in Inorganic Materials*. Cambridge University Press, 2014.

[30] Nicolas Eustathopoulos, Michael G Nicholas, and Béatrice Drevet. *Wettability at high temperatures*, volume 3. Elsevier, 1999.

[31] JJ Bikerman. Proceedings of the second international congress of surface activity. vol. iii: Electrical phenomena. solid/liquid interface, 621 pp., 1958.

[32] JP Garandet, B Drevet, and N Eustathopoulos. On the validity of youngs equation in the presence of gravitational and other external force fields. *Scripta materialia*, 38(9):1391–1397, 1998.

[33] Akira Nakajima, Kazuhito Hashimoto, and Toshiya Watanabe. Recent studies on super-hydrophobic films. *Monatshefte für Chemie/Chemical Monthly*, 132(1):31–41, 2001.

[34] Robert N Wenzel. Resistance of solid surfaces to wetting by water. *Industrial & Engineering Chemistry*, 28(8):988–994, 1936.

[35] C Yang, U Tartaglino, and BNJ Persson. Influence of surface roughness on superhydrophobicity. *Physical review letters*, 97(11):116103, 2006.

[36] Taolei Sun, Lin Feng, Xuefeng Gao, and Lei Jiang. Bioinspired surfaces with special wettability. *Accounts of Chemical Research*, 39(7):487–487, 2006.

[37] Pierre-Gilles De Gennes, Francoise Brochard-Wyart, and David Quere. *Capillarity and wetting phenomena: drops, bubbles, pearls, waves*. Springer Science & Business Media, 2013.

[38] Elena Martines, Kris Seunarine, Hywel Morgan, Nikolaj Gadegaard, Chris DW Wilkinson, and Mathis O Riehle. Superhydrophobicity and superhydrophilicity of regular nanopatterns. *Nano letters*, 5(10):2097–2103, 2005.

[39] Jean Berthier and Ken Brakke. *The physics of microdroplets*. John Wiley & Sons, 2012.

[40] Jean Berthier. *Micro-drops and digital microfluidics*. William Andrew, 2012.

[41] Jose Bico, Uwe Thiele, and David Quere. Wetting of textured surfaces. *Colloids and Surfaces A: Physicochemical and Engineering Aspects*, 206(1):41–46, 2002.

[42] Daiki Murakami, Hiroshi Jinnai, and Atsushi Takahara. Wetting transition from the cassie–baxter state to the wenzel state on textured polymer surfaces. *Langmuir*, 30(8):2061–2067, 2014.

[43] Rulon E Johnson Jr and Robert H Dettre. Contact angle hysteresis. iii. study of an idealized heterogeneous surface. *The journal of physical chemistry*, 68(7):1744–1750, 1964.

[44] Alberto Giacomello, Simone Meloni, Mauro Chinappi, and Carlo Massimo Casciola. Cassie–baxter and wenzel states on a nanostructured surface: phase diagram, metastabilities, and transition mechanism by atomistic free energy calculations. *Langmuir*, 28(29):10764–10772, 2012.

[45] Gene Whyman, Edward Bormashenko, and Tamir Stein. The rigorous derivation of young, cassie–baxter and wenzel equations and the analysis of the contact angle hysteresis phenomenon. *Chemical Physics Letters*, 450(4):355–359, 2008.

[46] Aurelie Lafuma and David Quere. Superhydrophobic states. *Nature materials*, 2(7):457–460, 2003.

[47] ABD Cassie and S Baxter. Wettability of porous surfaces. *Transactions of the Faraday Society*, 40:546–551, 1944.

[48] Neelesh A Patankar. On the modeling of hydrophobic contact angles on rough surfaces. *Langmuir*, 19(4):1249–1253, 2003.

[49] P Roura and J Fort. Comment on effects of the surface roughness on sliding angles of water droplets on superhydrophobic surfaces. *Langmuir*, 18(2):566–569, 2002.

[50] Barry Arkles. Hydrophobicity, hydrophilicity and silanes. *Paint & Coatings Industry magazine*, 2006.

[51] Barry Arkles. Hydrophobicity, hydrophilicity and silane surface modification. *Gelest, Inc. Available at http://www.gelest.com/goods/pdf/hydrophobicity.pdf*, 2006.

[52] George Wypych. *Handbook of solvents*. ChemTec Publishing, 2001.

[53] Robert C Weast. Handbook of chemistry and physics, cleveland. *CRC Press, Inc*, 1975:E58, 1974.

[54] Paul M Dewick. *Essentials of organic chemistry: for students of pharmacy, medicinal chemistry and biological chemistry*. John Wiley & Sons, 2006.

[55] Grace Materials Technologies. Ludox® colloidal silica, product information. Technical report, W. R. Grace & Co.-Conn., 2012.

[56] Grace Davison Engineered Materials. Ludox® colloidal silica in coatings lithium polysilicate in coatings, technical information. Technical report, W.R. Grace & Co.-Conn., 2007.

[57] David O'Hagan. Understanding organofluorine chemistry. an introduction to the c–f bond. *Chemical Society Reviews*, 37(2):308–319, 2008.

[58] Werner Kern. The evolution of silicon wafer cleaning technology. *Journal of the Electrochemical Society*, 137(6):1887–1892, 1990.

[59] Sheng-Hsiang Tseng, Fu-Yuan Xiao, Ying-Zong Juang, and Chin-Fong Chiu. Methods for dicing a released cmos-mems multi-project wafer, October 14 2008. US Patent 7,435,663.

[60] Hao Feng, Gustavo V Barbosa-Canovas, and Jochen Weiss. *Ultrasound technologies for food and bioprocessing*, volume 1. Springer, 2011.

[61] Quan Qi and Giles J Brereton. Mechanisms of removal of micron-sized particles by high-frequency ultrasonic waves. *Ultrasonics, Ferroelectrics, and Frequency Control, IEEE Transactions on*, 42(4):619–629, 1995.

[62] VB Menon, LD Michaels, RP Donovan, VL Debler, and MB Ranade. Particle removal from semiconductor wafers using cleaning solvents. In *Particles in Gases and Liquids 1*, pages 259–271. Springer, 1989.

[63] Werner Kern et al. Handbook of semiconductor wafer cleaning technology. *New Jersey: Noyes Publication*, pages 111–196, 1993.

[64] John R Vig. Uv/ozone cleaning of surfaces. *Journal of Vacuum Science & Technology A*, 3(3):1027–1034, 1985.

[65] LTD Three Bond Co. Ultraviolet-ozone surface treatment. Technical report, Three Bond Technical News, March 20 1987.

[66] Leo Zafonte and Rafael Chiu. Uv/ozone cleaning for organics removal on silicon wafers. In *1984 Microlithography Conferences*, pages 164–177. International Society for Optics and Photonics, 1984.

[67] Christiane Gottschalk and Juergen Schweckendiek. Using dissolved ozone in semiconductor cleaning applications. *Paper reprinted from MICRO, Canon Communications LLC Publication, March*, 2004.

[68] Rohm and Haas. Microposit(tm) s1800(tm) series photoresist, 2006.

[69] Aurélien F Stalder, Tobias Melchior, Michael Müller, Daniel Sage, Thierry Blu, and Michael Unser. Low-bond axisymmetric drop shape analysis for surface tension and contact angle measurements of sessile drops. *Colloids and Surfaces A: Physicochemical and Engineering Aspects*, 364(1):72–81, 2010.

[70] Daeyeon Lee, Zekeriyya Gemici, Michael F Rubner, and Robert E Cohen. Multilayers of oppositely charged sio2 nanoparticles: effect of surface charge on multilayer assembly. *Langmuir*, 23(17):8833–8837, 2007.

[71] Sneha A Kulkarni, Satishchandra B Ogale, and Kunjukrishanan P Vijayamohanan. Tuning the hydrophobic properties of silica particles by surface silanization using mixed self-assembled monolayers. *Journal of colloid and interface science*, 318(2):372–379, 2008.

[72] Hitoshi Ogihara, Jing Xie, Jun Okagaki, and Tetsuo Saji. Simple method for preparing superhydrophobic paper: spray-deposited hydrophobic silica nanoparticle coatings exhibit high water-repellency and transparency. *Langmuir*, 28(10):4605–4608, 2012.

[73] Microchemicals GmbH. *Photoresist Removal*, 2013. Available on http://www.microchemicals.com/downloads/application_notes.html.

[74] Microchemicals GmbH. *Solvents: Theory and Application*, 2013. Available on http://www.microchemicals.com/downloads/application_notes.html.

[75] Barbara Kanegsberg and Ed Kanegsberg. *Troubleshooting Your Ultrasonic Cleaning Process*. Materials Today, by ELESEVIER, 2009.

[76] Tommaso Baldacchini, James E Carey, Ming Zhou, and Eric Mazur. Superhydrophobic surfaces prepared by microstructuring of silicon using a femtosecond laser. *Langmuir*, 22(11):4917–4919, 2006.

[77] Frank Meiners, Jan Henning Ross, Izabella Brand, Anna Buling, Manfred Neumann, Philipp Julian Köster, Jens Christoffers, and Gunther Wittstock. Modification of silicon oxide surfaces by monolayers of an oligoethylene glycol-terminated perfluoroalkyl silane. *Colloids and Surfaces A: Physicochemical and Engineering Aspects*, 449:31–41, 2014.

[78] Mingji Wang, Kenneth M Liechti, Qi Wang, and JM White. Self-assembled silane monolayers: fabrication with nanoscale uniformity. *Langmuir*, 21(5):1848–1857, 2005.

[79] Hiroaki Tada and Hirotsugu Nagayama. Chemical vapor surface modification of porous glass with fluoroalkyl-functional silanes. 1. characterization of the molecular layer. *Langmuir*, 10(5):1472–1476, 1994.

[80] RE Geer, DA Stenger, MS Chen, JM Calvert, R Shashidhar, YH Jeong, and Peter S Pershan. X-ray and ellipsometric studies of self-assembled monolayers of fluorinated chlorosilanes. *Langmuir*, 10(4):1171–1176, 1994.

[81] Reena Banga, Jack Yarwood, Anthony M Morgan, Brian Evans, and Jaqueline Kells. Ftir and afm studies of the kinetics and self-assembly of alkyltrichlorosilanes and (perfluoroalkyl) trichlorosilanes onto glass and silicon. *Langmuir*, 11(11):4393–4399, 1995.

[82] Dirk G Kurth and Thomas Bein. Surface reactions on thin layers of silane coupling agents. *Langmuir*, 9(11):2965–2973, 1993.

[83] Dirk G Kurth and Thomas Bein. Monomolecular layers and thin films of silane coupling agents by vapor-phase adsorption on oxidized aluminum. *The Journal of Physical Chemistry*, 96(16):6707–6712, 1992.

[84] PIKE Technologies. Atr - theory and applications, 2011.

[85] Christian Reichardt and Thomas Welton. *Solvents and solvent effects in organic chemistry*. John Wiley & Sons, 2011.

[86] Masashi Miwa, Akira Nakajima, Akira Fujishima, Kazuhito Hashimoto, and Toshiya Watanabe. Effects of the surface roughness on sliding angles of water droplets on superhydrophobic surfaces. *Langmuir*, 16(13):5754–5760, 2000.

[87] Jaroslaw Drelich. The effect of drop (bubble) size on contact angle at solid surfaces. *The Journal of Adhesion*, 63(1-3):31–51, 1997.

[88] Abraham Marmur. Soft contact: measurement and interpretation of contact angles. *Soft Matter*, 2(1):12–17, 2006.

[89] Nicolas J Harrick. *Internal reflection spectroscopy*. Harrick Scientific Corp., 1967.

[90] Nesrine Aissaoui, Latifa Bergaoui, Jessem Landoulsi, Jean-François Lambert, and Souhir Boujday. Silane layers on silicon surfaces: mechanism of interaction, stability, and influence on protein adsorption. *Langmuir*, 28(1):656–665, 2011.

[91] Yang Leng. *Materials characterization: introduction to microscopic and spectroscopic methods*. John Wiley & Sons, 2009.

[92] Barbara Stuart. *Infrared spectroscopy*. Wiley Online Library, 2005.

[93] Brian C Smith. *Fundamentals of Fourier transform infrared spectroscopy*. CRC press, 2011.

[94] Andrew R Hind, Suresh K Bhargava, and Anthony McKinnon. At the solid/liquid interface: Ftir/atr the tool of choice. *Advances in colloid and interface science*, 93(1):91–114, 2001.

[95] KiRyong Ha, Wonsool Ahn, Seungbaik Rho, Soonghyuck Suh, Dongsu Synn, Martin Stelzle, and John F Rabolt. Characterization of orientation of perfluorostearic acid langmuir–blodgett multilayers by infrared spectroscopic methods. *Thin Solid Films*, 372(1):223–229, 2000.

[96] Jem-Kun Chen, Fu-Hsiang Ko, Kuen-Fong Hsieh, Cheng-Tung Chou, and Feng-Chih Chang. Effect of fluoroalkyl substituents on the reactions of alkylchlorosilanes with mold surfaces for nanoimprint lithography. *Journal of Vacuum Science & Technology B*, 22(6):3233–3241, 2004.

[97] LE Fernandez, A Ben Altabef, and EL Varetti. The force constants in the isoelectronic series CF_3SO_2X (x=F, OH, NH_2, CH_3): a study based on dft calculations and experimental data. *Journal of molecular structure*, 612(1):1–11, 2002.

[98] LE Fernandez and EL Varetti. An experimental and theoretical study of the vibrational properties of CF_3SO_2Cl. *The Journal of the Argentine Chemical Society*, 97(1):199–209, 2009.

[99] Gertjan Koster and Guus Rijnders. *In situ characterization of thin film growth*. Elsevier, 2011.

[100] Toru Yoshizawa. *Handbook of optical metrology: Principles and Applications*. CRC Press, 2009.

[101] Vito DePalma and Nolan Tillman. Friction and wear of self-assembled trichlorosilane monolayer films on silicon. *Langmuir*, 5(3):868–872, 1989.

[102] Sanjay S Latthe, Hiroaki Imai, V Ganesan, and A Venkateswara Rao. Superhydrophobic silica films by sol–gel co-precursor method. *Applied Surface Science*, 256(1):217–222, 2009.

[103] Tao Ning, Wenguo Xu, and Shixiang Lu. Fabrication of superhydrophobic surfaces on zinc substrates and their application as effective corrosion barriers. *Applied Surface Science*, 258(4):1359–1365, 2011.

[104] Tian He, Yuanchao Wang, Yijian Zhang, Tugen Xu, Tao Liu, et al. Super-hydrophobic surface treatment as corrosion protection for aluminum in seawater. *Corrosion science*, 51(8):1757–1761, 2009.

[105] Tao Liu, Shougang Chen, Sha Cheng, Jintao Tian, Xueting Chang, and Yansheng Yin. Corrosion behavior of super-hydrophobic surface on copper in seawater. *Electrochimica Acta*, 52(28):8003–8007, 2007.

[106] Tao Liu, Kin Tak Lau, Shou Gang Chen, Sha Cheng, and Yan Sheng Yin. Super-hydrophobic surfaces improve corrosion resistance of Fe_3Al-type intermetallic in seawater. In *Advanced Materials Research*, volume 47, pages 173–176. Trans Tech Publ, 2008.

[107] Yansheng Yin, Tao Liu, Shougang Chen, Tong Liu, and Sha Cheng. Structure stability and corrosion inhibition of super-hydrophobic film on aluminum in seawater. *Applied Surface Science*, 255(5):2978–2984, 2008.

[108] Dongyun Yu, Jintao Tian, Jinhui Dai, and Xin Wang. Corrosion resistance of three-layer superhydrophobic composite coating on carbon steel in seawater. *Electrochimica Acta*, 97:409–419, 2013.

[109] Zhiguang Guo, Feng Zhou, Jingcheng Hao, and Weimin Liu. Stable biomimetic super-hydrophobic engineering materials. *Journal of the American Chemical Society*, 127(45):15670–15671, 2005.

[110] Baitai Qian and Ziqiu Shen. Fabrication of superhydrophobic surfaces by dislocation-selective chemical etching on aluminum, copper, and zinc substrates. *Langmuir*, 21(20):9007–9009, 2005.

[111] DK Sarkar, M Farzaneh, and RW Paynter. Superhydrophobic properties of ultrathin rf-sputtered teflon films coated etched aluminum surfaces. *Materials letters*, 62(8):1226–1229, 2008.